Ocean Engineering 261 (2022) 111688

Contents lists available at ScienceDirect

Ocean Engineering

journal homepage: www.elsevier.com/locate/oceaneng

# Sail-induced resistance on a wind-powered cargo ship

Jarle Vinje Kramer *, Sverre Steen

*Department of Marine Technology, Norwegian University of Science and Technology, Otto Nielsens veg 10, 7052, Trondheim, Norway*

ARTICLE INFO

*Keywords:*
Wind-power
CFD
Discrete lifting line
Route simulation
Hydrodynamic design

ABSTRACT

This article explores the added resistance due to side forces from wingsails, called the sail-induced resistance. A cargo ship is tested with varying speed, appendages, number of sails, and control algorithms for the sails. The appendages consist of bilge keels, a high aspect-ratio fixed keel, and a dynamically controlled keel. The sails were controlled both to maximize the thrust and to iteratively optimize the angle of attack including hydrodynamic effects. The physical modelling was done with a combination of CFD, maneuvering theory, discrete lifting line, and empirical models. The magnitude of the sail-induced resistance without any keels was found to be comparable to the added resistance in waves. The main source of the resistance was the rudder, which was forced to operate at large angles in steady state conditions. Adding the appendages reduced the sail-induced resistance, but the fixed appendages also increased the friction. The dynamic keel was therefore the only appendage that significantly improved the fuel savings. The side force from the sails could be significantly reduced with limits in the control algorithm. Although this limit also reduced the thrust from the sails, the fuel savings remained high due to a roughly equal reduction in the sail-induced resistance.

## 1. Introduction

Modern sail technologies have the potential to significantly reduce the energy consumption of cargo vessels. The popularity of the technology is therefore increasing, both in the scientific literature and in the maritime industry. Several ships have recently installed wind-power devices, and more projects are planned for the near future. Examples include the general cargo ship SC Connector that recently installed two 35 m tall rotor sails (Ship Technology, 2021), the general cargo ship MV Ankie that have installed two 10 m tall suction sails (Econowind, 2020), and the planned car carrier Ocean Bird that is designed with four 80 m tall wingsails (Wallenius Marien and Alfa Laval, 2021). Although there are clear benefits with sails, they also come with new challenges for the design and operation of the ships that use them. A well-known problem is the direction of the force that is created from the wind: depending on the apparent wind angle relative to the ship direction, there is often a side force component from the sails that is several times larger than the thrust. If the ship is to move with a steady velocity and heading, this aerodynamic side force must be balanced with opposing hydrodynamic forces from the hull and the rudder. To achieve this, the ship must be operated with a steady drift angle – also known as leeway angle - and rudder angle. As a result, the resistance of the vessel is increased. This increase in resistance can in some cases reduce the benefit from the sails considerably. We refer to this added resistance as the *sail-induced* resistance, defined as the resistance on the ship with sails minus the resistance without sails at the same velocity. This article explores three questions related to this resistance component:

- How large is the sail-induced resistance on a wind-powered cargo ship?
- What is the main source of the resistance?
- How can the sail-induced resistance be reduced?

To answer these questions, we performed a case study of a cargo ship equipped with several large wingsails on a coastal route in northern Europe. The hydrodynamic forces as a function of drift angle, rudder angle, propeller loading, and ship speed was analyzed with Computational Fluid Dynamics (CFD). The results from these simulations were used to generate a hydrodynamic route simulation model based on maneuvering theory. The sails were analyzed with a discrete lifting line method that includes interaction effects between multiple wings. The propeller and the added resistance in waves were analyzed using empirical methods. All models were combined with weather data using a route simulation framework. Numerical solvers ensured balance between the aerodynamic and the hydrodynamic forces and moments in 4 degrees of freedom: surge, sway, roll and yaw. Table 1 shows a list of

* Corresponding author.
*E-mail address:* jarle.a.kramer@ntnu.no (J. Vinje Kramer).

https://doi.org/10.1016/j.oceaneng.2022.111688
Received 2 February 2022; Received in revised form 2 May 2022; Accepted 29 May 2022
Available online 19 August 2022

**Table 1**
Physical effects in this case study.

| Domain | Effects included | Effects neglected |
|---|---|---|
| **Hydrodynamics** | - Calm water resistance<br>- Drift forces<br>- Rudder forces<br>- Drift and rudder coupling effects<br>- Heel angle<br>- Propeller efficiency<br>- Interaction between rudder, hull, and propeller<br>- Added resistance due to ocean waves | - Dynamic sinkage and trim<br>- Heel and drift coupling effects<br>- Drift effects on the propeller<br>- Side force and yaw moment from ocean waves |
| **Aerodynamics** | - Viscous effects on lift and drag on the wingsails<br>- Lift-induced effects on lift and drag<br>- Interaction effects between multiple sails<br>- Optimized operation policy | - Interaction between sails and ship superstructure<br>- Aerodynamic forces on the superstructure<br>- Height variation in wind direction<br>- Aerodynamic damping of ship motion in waves<br>- Dynamic effects such as gusts and sudden weather changes |
| **Ship operation** | - Coastal route with hindcast weather data<br>- Limits on the sail control to avoid capsizing<br>- Limits on the sail control to avoid loss of steering | - Details in the logistics of the route, such as variation in cargo and time schedule<br>- Maneuvering in harbors<br>- Short term dynamics from control systems, such as the sails influence on the autopilot |

physical effects that are included or neglected in the simulation, with more details described throughout the article.

The importance of the sail-induced resistance is dependent on several factors. In this paper, we vary the hydrodynamic design of the ship, the operational speed, the total sail area, and the control policy of the sails. The number of sails is varied between 1 and 5 and the design speed is varied between 8 and 16 knots. The number of sails vary the magnitude of both the thrust and the side force from the sails. The variation in the ship velocity varies both the ship resistance and the apparent wind angle.

The variation due to the physical design was evaluated by testing four different ship configurations. A bare hull with a spade rudder was the base-line design. We then tested the effect of three different keel-designs, all intended to increase the side-force-to-drag ratio of the ship: low aspect-ratio bilge keels, a static high aspect-ratio keel, and a dynamic keel that is both retractable and where the angle of attack can be adjusted. The main purpose of adding the bilge keels was to move the center of lateral resistance – also known as the hydrodynamic center of effort – backwards on the hull. For the bare hull, the rudder was generally forced to operate with large angles to keep the ship balanced in yaw. This created a large increase in the resistance on the rudder. Adding the bilge keels was an attempt to reduce the required rudder angle, and therefore the rudder resistance. The high aspect-ratio keels were tested as the lift-induced resistance generally decrease rapidly with an increasing aspect-ratio of the lifting surface. They were therefore expected to improve the side-force-to-drag-ratio relative to the low aspect-ratio hull. The dynamic keel was introduced to decouple the side force on the keel from the drift angle of the vessel, and thereby allow more of the side force to be balanced by the high aspect-ratio keel.

Two different control policies were tested. The first policy always maximizes the thrust from the sails. The second policy iteratively optimizes the angle of attack to maximize the thrust minus the sail-induced resistance. The full hydrodynamic route simulation model is used in the optimization procedure for the second policy. The purpose was to quantify how much the sail-induced resistance is dependent on the control algorithm of the sails. For both algorithms, explicit limits on the side force, rudder angle, and heel angle are used to ensure safe and realistic operation of the ship. To explore a simple way to manage the sail-induced resistance, we also investigated the effect of varying the value of side force limit for both control algorithms.

When analyzing wind-powered ships, the primary goal is usually to quantify the fuel savings due to the sails. This involves some form of route simulation which combines models of the ship with weather data. There is currently a large variation in model complexity and assumptions between different papers on this topic. Although the concept of the sail-induced resistance is text-book knowledge for sailboats (Larsson et al., 2000), it has been common to neglect this effect when analyzing merchant ships. Examples of scientific papers from the last decade using this simplification can for instance be found in (Ouchi et al., 2011), (Traut et al., 2014), (Bøckmann et al., 2014), (Yuankui et al., 2014), (Bentin et al., 2016), (Talluri et al., 2016) and (Talluri et al., 2018). The papers investigate the fuel savings due to rotor sails, wingsails, wind turbines and kites using different route simulation frameworks. Most of these examples only include the calm water straight-ahead resistance in the hydrodynamic model, while one also includes the added resistance in waves. Whether the sail-induced resistance is neglected due to the added complexity or because it is assumed to be a negligible resistance component is not explicitly stated by the authors. The interest in the sail-induced resistance for merchant ships has, however, increased recently. Examples of route simulations where the sail-induced resistance is included can be found in (Tillig and Ringsberg, 2020), (Lu and Ringsberg, 2020) and (van der Kolk et al., 2019). The papers analyze different ships with rotor sails and the hydrodynamic models are based on either empirical expressions or CFD simulations of the ship. A dedicated paper about hydrodynamic CFD-simulations of wind-powered ships can be found in (van der Kolk et al., 2020). The focus is on efficient meshing strategies and turbulence models, to facilitate efficient hydrodynamic testing of wind-powered ships.

Although these references fully acknowledge the negative hydrodynamic effects related to wind-power, they do not focus directly on the importance of the sail-induced resistance. Rather, it is either only a part of a larger resistance model used to explore the benefit of wind-power, or the focus is on the technical requirements for the hydrodynamic modelling. Although this resistance is clearly important for sailboats – especially for vessels intended for high speed – there are some differences for merchant ships. On one hand, merchant ships are generally hybrid ships, where only part of the propulsion comes from the wind. This suggest that the sail-induced resistance may not be that large in many cases. On the other hand, merchant ships are not designed for balancing large side forces. This could mean that even relatively small side forces could lead to problems. The magnitude of the sail-induced resistance is a good indicator for whether changes should be made to the hydrodynamic design. If it is large, ship designers working on wind-powered ships should update the hull and appendage design to balance the side force more efficiently. If it is small, they can largely continue with the same designs as today.

There have been some hydrodynamic design investigations of wind-powered merchant ships in the literature previously. An example is (van der Kolk et al., 2021), which present results from a large experimental study of low-aspect-ratio bilge keels. The goal was to see how much the keels could improve the ship's ability to balance the side forces from sails. The paper presents results for the hydrodynamic side force, resistance, and center of lateral resistance, as a function of drift angle. However, it does not include any analysis of aerodynamic forces or route simulations to quantify the actual improvements during operation. An example of a design exploration that do include route simulations is presented in (Minami et al., 2003). The paper explores the effect of adding different shallow keels to a wind-powered merchant ship. The main goal was to reduce the rudder angle to maintain steerability in

unfavorable weather conditions. The authors stated that they were initially worried that adding the keels would increase the fuel consumption due to the added friction. The results show that the fuel savings from the sails are not much affected by the keels, but that the rudder angle was reduced. The keels are therefore seen to reduce the average sail-induced resistance roughly as much as they increase the frictional resistance.

Variations in the control algorithm for sails have also been studied previously. The work presented in (Sacher et al., 2015) and (Aubin et al., 2017) explores how the shape of soft sails can be optimized including a simple method for accounting for the negative hydrodynamic effects due to the sails. A penalty that is proportional to the side force from the sails is added in the objective function in the optimization. However, the focus of the papers is on the aerodynamic testing and the optimal value of the linear penalty is therefore not evaluated directly.

We have previously done a smaller but similar study as the one presented in this paper, found in (Kramer and Steen, 2016). The conclusion then was that the sail-induced resistance had a large impact on the fuel savings for a wind-powered merchant ship, and that the control strategy for the sails should be optimized with hydrodynamic effects included in the objective function. However, the previous study was based on a simplified model of the ship, the sails, and the control algorithm. The current paper can in some ways be seen as a significantly updated version of (Kramer and Steen, 2016), which resulted in somewhat different conclusions.

The structure of the article is as follows: details of the case study are given in Section 2, the CFD setup is explained in Section 3, the hydrodynamic modelling framework in Section 4, the aerodynamic modelling framework in Section 5, and the route simulation framework in Section 6. The results and conclusion are then presented in Section 7 and 8. We show how the hydrodynamic resistance of the different design variants depends on an externally applied side force and which part of the ship – the hull, the rudder, or the keel – experiences the largest resistance. Results from route simulations are used to measure how much the fuel savings due to wind-power are reduced due to the negative hydrodynamic effects and we compare the sail-induced resistance against all the other resistance components on the ship. Finally, we compare the difference between the two control algorithms and the effect of varying the side force limit on the sails.

## 2. Case study details

The ship design used in this case study was intended to represent a simple yet typical cargo ship with roughly 5000 tons dead weight capacity (DWT). The exact cargo type is not considered directly, but we imagine either a coastal general cargo ship or a dry bulker. The features of the ship that are kept constant throughout the case study are presented in Section 2.1 before the different appendages are explained in section 2.2. An illustration of the hydrodynamic design features along with main dimensions of the ship is shown in Fig. 2. This figure also includes the coordinate system used when evaluating the hydrodynamic forces and moments. The sails and super structure of the ship are illustrated in Fig. 1.

### 2.1. Fixed features

#### 2.1.1. Main dimensions

The values for the length, width, depth, and displacement of the ship are based on similar reference ships with significant rounding on all values. The fully loaded mass of the ship is 9000 tones. The ratio between deadweight and loaded displacement for a cargo ship will vary based both on type and size of the ship. Schneekluth and Bertram (1998) state that this ratio is often between 60 and 80% for general cargo ships with 5000–15 000 DWT. We chose a slightly lower ratio of roughly 55%, based on numbers from a previous commercial project at our department. The rudder planform area is right above 2% of the underwater hull lateral area, calculated as the ship's length multiplied by depth. As a comparison, Bertram (2012) states that this variable is typically around 1.5% for cargo ships.

#### 2.1.2. Speed and power

The design speed of the ship was varied between 8 and 16 knots, with a step size of 2 knots. Each design speed is assumed to represent a different ship where the engine size is adjusted to the required power. The maximum engine power is a variable that is used to determine involuntary speed loss. The engine size is adjusted based on the calm water resistance, the propulsion efficiency of the propeller, an assumed sea margin of 30%, and an engine design load of 80%. The resulting power is 530, 1 100, 2 100, 3400 and 5700 kW for the ship speeds 8, 10, 12, 14 and 16 knots respectively. Data for the hull resistance and propeller efficiency will be presented later in the text. The propeller diameter was the same for all speeds and design configurations. The size corresponds to a thrust loading coefficient in calm water between 0.4 and 0.53 depending on the design variant and speed. The thrust loading coefficient is defined as $C_{T,p} = T / (0.5\,\rho\,A_p\,U_s^2)$, where $T$ is the propeller thrust, $\rho$ the water density, $A_p$ the propeller disk area and $U_s$ the ship speed.

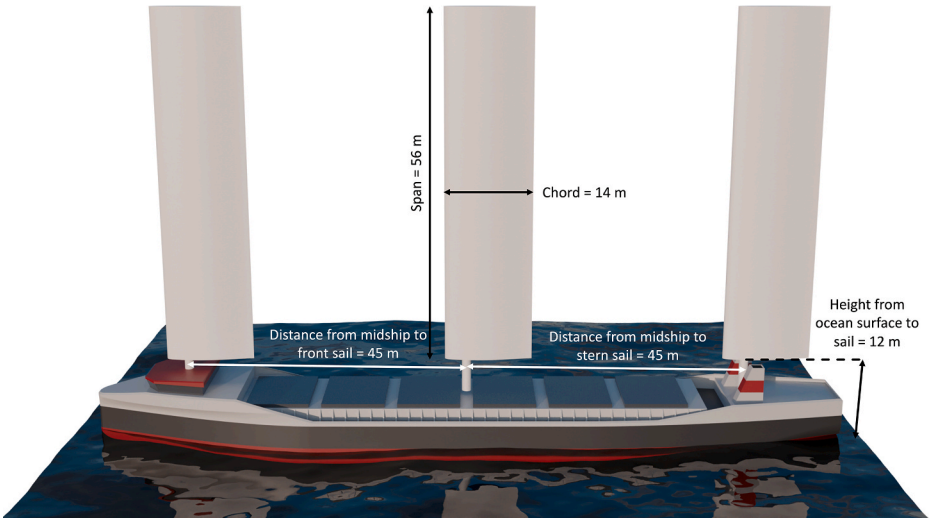


**Fig. 1.** Illustration of the superstructure and sail geometry used for this case study.

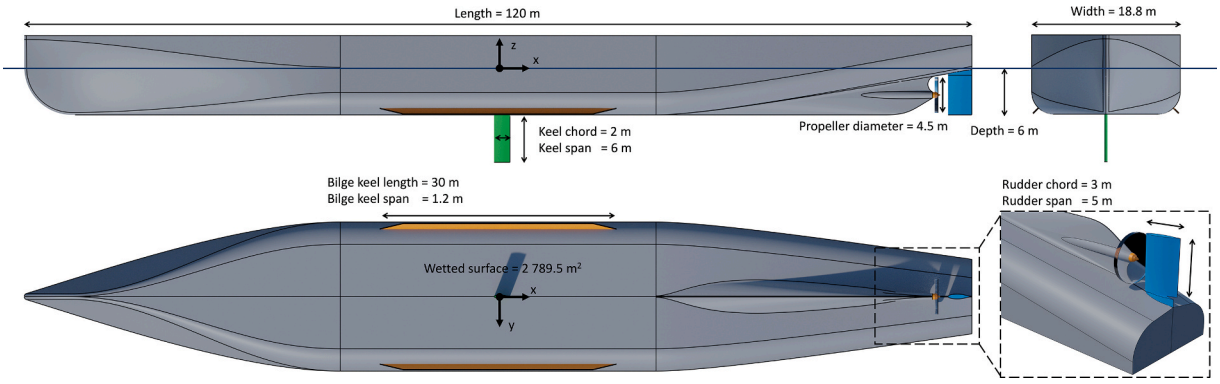


**Fig. 2.** Hydrodynamic design overview. The ship is shown with all appendages installed.

#### 2.1.3. Stability

The ship was assumed to have a relatively high stability as the primary interest in this study was the lift and lift-induced drag due to drift and rudder angles. Limiting the heel angle allows for practical simplifications on the hydrodynamic model, which are addressed later in the text. According to (Schneekluth and Bertram, 1998), recommended values for the minimum initial metacentric height (GM) in fully loaded conditions varies between 0.8 m and 1.0 m for general cargo ships. Dry bulkers can have significantly higher values due to heavy cargo placed low in the hull. Based on data from commercial projects at our department, we know of general cargo ships of similar size as our case study ship that typically operate with a GM between 1.0 m and 2.0 m, depending on the cargo. We have therefore assumed a GM value of 1.5 m for this case study. The heel angles during the route simulation are calculated based on this value and an initial linear stability model for the hull: the restoring heel moment is defined as $M_x = GM\,\varphi\,g\,\Delta$, where $\varphi$ is the heel angle, $g$ the acceleration of gravity, and $\Delta$ the mass displacement of the ship. In addition, the hydrodynamic heel moment from the rudder and the keel is calculated based on the side force they produce at a given weather condition and a fixed center of effort at the midspan of each appendage. The heel moment from the appendages is generally destabilizing since the vertical center of effort is below the center of gravity of the ship. However, the importance of the appendages for the heel angle was small in this case study due to the relative magnitude of the hydrostatic moment on the hull. Details on how the side force from the appendages is calculated will be given in Section 4 and values for the heel angle during route simulations will be presented in Section 7.

#### 2.1.4. Sails and superstructure

The sails in the case study were solid single element symmetric wingsails with a NACA 0015 foil profile. The dimensions of the sails were manually adjusted to achieve well above 50% reduction in fuel consumption on average for the lowest test speeds on a case study route between Trondheim and Rotterdam. More information regarding the route and weather data will be given in Section 6.2. The placement was such that the average location of the quarter chord is always midship. The sails are assumed to be retractable, for instance by using a telescopic mechanism. When the sails are retracted, the area is reduced to a quarter of the full size in the aerodynamic model, to minimize the drag force. When to retract is governed by the control algorithm for the sails, which will be presented in Section 6.1.2. Retractability can be a challenging design feature that is not necessarily used on vessels with small sails. However, both existing and planned vessels with larger sails seem to value this feature enough to include the added complexity. Examples of modern retractable sails include the telescopic wingsails in the Ocean Bird project (Wallenius Marien and Alfa Laval, 2021), the foldable wingsails from Ayro and VPLP (Ayro, 2022), the tiltable rotor sails from Norsepower on the ship SC connector (Ship Technology, 2021), and the inflatable wingsails from Michelin (2021).

### 2.2. Appendages

#### 2.2.1. Bilge keels

A solution for improving the ship's ability to balance side forces is bilge keels. This is also a design feature that is already installed on many merchant ships for seakeeping purposes. As mentioned in the introduction, this design feature is explored experimentally for wind-powered ships in (van der Kolk et al., 2021). Although the paper clearly showed that bilge keels would increase the side force and move the hydrodynamic center of lateral resistance backwards for a given drift angle, it was unclear exactly how much the fuel savings for a wind-powered ship would change. We therefore decided to explore this further in this study. Inspired by the results in (van der Kolk et al., 2021), we used relatively short bilge keels. The difference in the center of lateral resistance for long and short bilge keels was shown to not be very dependent on the length and shorter bilge keels will add less frictional resistance when moving straight-ahead. The intended functionality of bilge keels is to ensure separation around the bottom edge of the ship. To have this effect, it is important that the edge of the bilge keels extend outside the boundary layer. The height of the bilge keels is dimensioned based on an empirical estimation of the boundary layer thickness, $\delta$, and a safety factor. The Schlichting equation (Schlichting, 1979) was used, which states that the turbulent boundary layer thickness depends on the Reynolds number, $Re_x$, calculated based on the length from the bow to the location where the thickness is evaluated, $x$. The expression is given as $\delta = 0.37\,x\,/Re_x^{1/5}$ . The CFD simulations in this paper were done in model scale 1:4. The reduced scale was chosen as a practical compromise between scaling accuracy and computational speed based on previous work (Kramer and Steen, 2022). The boundary layer thickness furthest back at the bilge keels in model scale 1:4 was estimated to be 0.2 m, which corresponds to 0.8 m with simple geometrical scaling to full-scale. We then assumed a safety factor 1.5 and set the height of the full-scale bilge keels to 1.2 m.

#### 2.2.2. High aspect-ratio keel

With inspiration from conventional sailboats, high aspect-ratio keels are a natural design feature to consider for wind-powered cargo ships. However, the increased depth due to a keel can in some cases be problematic. For instance, in our hometown of Trondheim, there are several cargo ports that have a maximum depth of 8 m. The case study ship tested in this paper would therefore not be able to enter these ports with the static keel shown in Fig. 2. In addition, we also discovered that the fixed high aspect-ratio keel only had a limited impact on the sail-induced resistance – which is further addressed in Section 7.1. We therefore decided to also test a keel that could be dynamically controlled, using two mechanisms. First, the angle of the keel relative to the ship's centerline can be adjusted, like a rudder. Second, it can be retracted into the hull when it is not needed, similar to many types of roll stabilizing fins. It is controlled by an algorithm – further outlined in Section 6.1.3 –

that both determines when to deploy the keel and how large the operating angle should be for a given weather condition.

## 3. CFD simulations

CFD simulations were used for two tasks. First, it was used to simulate the hull, rudder, and keel together at various speeds, drift angles, rudder angles, and propeller loadings. This generated data that were further used to tune the hydrodynamic models in the route simulation framework presented in Section 4. Second, it was used to validate the lifting line model that was used to simulate the sails, presented in Section 5.

### 3.1. Overview of setup

The simulations were performed with the open-source software OpenFOAM, version 2006+ (ESI-Group, 2020). We used an internally developed software framework written in Python to automate and script all the details in the simulation setup. More details of the setup-procedure are presented in a recently published article found in (Kramer and Steen, 2022). The simulations for this study follow the same rules, and the explanation is therefore kept brief.

#### 3.1.1. Solvers and turbulence model

Two different OpenFOAM solvers are used. First, the solver simpleFoam is used for steady state single phase simulations. This includes hydrodynamic simulations for estimating forces that are assumed to not be dependent on free surface effects – such as forces due to drift and rudder angles – as well as aerodynamic simulations of the wingsails. Second, the solver interFoam is used to calculate the wave resistance on the ship. This solver uses the Volume of Fluid method (Hirt and Nichols, 1981) to capture the interaction between water and air. All simulations are performed with the turbulence model k-omega SST (Menter et al., 2003).

#### 3.1.2. Simulation domain and boundary conditions

An overview of the simulation domains is shown in Fig. 3. The size of the hydrodynamic domain is given relative to the ship length, L, while the size of the aerodynamic domain is given relative to the wingspan, S. The domain for the hydrodynamic simulations is shown in two different versions; one where the free surface is included in the simulation and one where it is simplified with the symmetry plane approximation. The symmetry plane approximation is referred to as double body simulations later in the text. When the free surface is included, wave damping zones based on the expressions in (Perić and Abdel-Maksoud, 2016) are used near the outer boundaries. The inlet values for the turbulent variables are based on recommended values from (Spalart and Rumsey, 2007) and an assumed turbulent intensity of 1%. Solid walls are modeled with continuous wall functions that blend between the logarithmic model and the viscous model using an exponential transition (Popovac and Hanjalic, 2007).

#### 3.1.3. Propeller model

The ship propeller is modeled as an actuator disk. The distribution of both thrust and torque is based on a theoretical Goldstein optimum distribution originally found in (Goldstein, 1929). Equations can also be found in (Kramer and Steen, 2022). The specific implementation of the actuator disk is based on a custom code for the OpenFOAM library, available in the online repository found in (Kramer, 2021). The relationship between thrust and torque is further based on the open water propeller data we assume for our analysis, further presented in Section 4.

### 3.2. Mesh

The mesh for the simulations is generated with snappyHexMesh – a meshing tool that is part of the OpenFOAM library. The resolution at different parts of the simulation domain is adjusted based on two main principles. The first principle adjusts the number of inflation layers close to solid walls so that the y + value reaches a target value of 60. The height of the first inflation layer is calculated based on a theoretical friction line and the Reynolds number of the tested geometry. The second principle adjusts the resolution in different parts of the domain relative to the representative length of the simulation. The chosen resolution is based on mesh convergence studies. More details of our mesh generation procedure can be found in (Kramer and Steen, 2022).

#### 3.2.1. Hydrodynamic mesh

An example of a mesh for the hydrodynamic simulations is shown in Fig. 4. All cell lengths are given relative to the ship length, L. The resolution at rudder was increased relative to the rest of the hull to better capture geometrical features. The resolution at the high aspect-ratio keel matches that of the rudder, while the bilge keels were refined to one level above the rest of the hull. The figure also shows the wake refinement zones, which vary slightly for cases with and without free surface. The difference is related to the need to capture waves generated by the ship. For cases with the free surface included, there is anisotropic vertical refinement in the region around the free surface to reduce the smearing of the volume fraction. The number of cells was approximately 9 and 12 million for double body cases without and with the high aspect-ratio keel respectively. The number of cells for the cases with the free surface included in the simulation was approximately 4.6 million. These simulations where only used to predict the straight-ahead resistance of the hull and therefore assumed symmetry across the centerline of the ship – i.e., with half the mesh size relative to cases where the side force is of interest.

Kramer and Steen (2022) contains an analysis of the uncertainty for

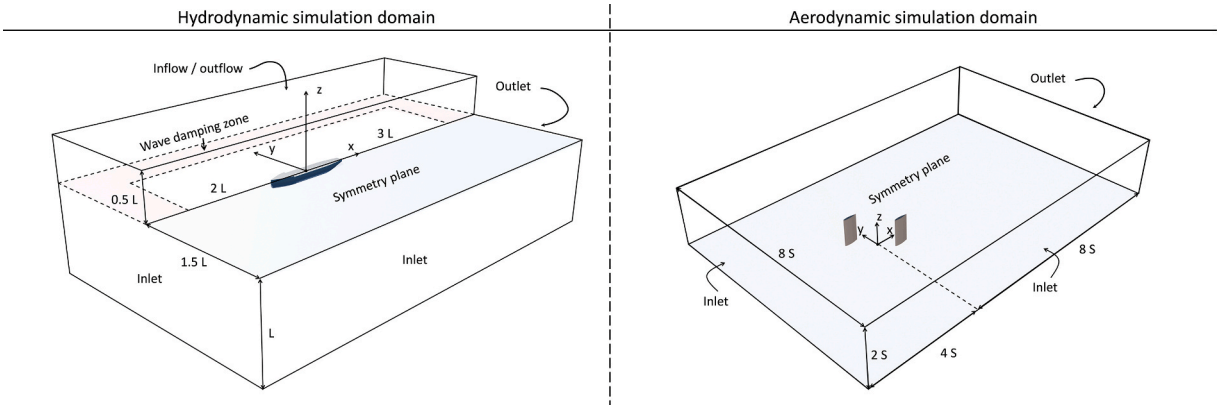


**Fig. 3.** Illustration of the simulation domain for both hydrodynamic and aerodynamic simulations.

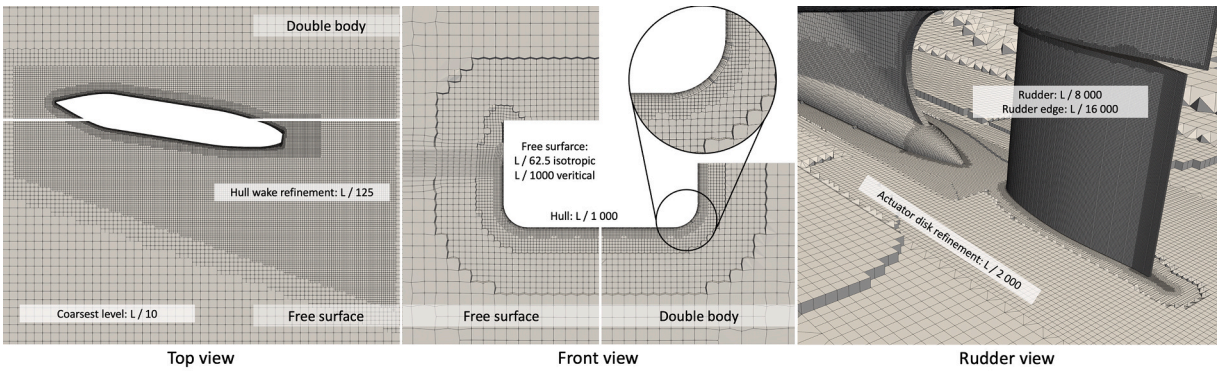


**Fig. 4.** Illustration of the hydrodynamic mesh with values for the cell lengths at different regions.

the hydrodynamic simulations using an identical simulation setup as the one used in this paper. This included convergence studies of both the mesh resolution and the time step, as well as comparisons against benchmark experiments. The mesh uncertainty for the hull forces at a drift angle equal to 9° was generally less than 2.5% for various model scales both with and without free surface modelling. The mesh uncertainty for the rudder-forces at a drift angle equal to 9° and rudder angle equal to 6° was generally less than 5%. The time step uncertainty was less than 1% for a ship hull moving with a drift angle equal to 9°. The calm-water, straight-ahead resistance was compared against three open ship geometries – KCS, KVLCC2 and DTMB 5415 – at Froude numbers varying from 0.1 to 0.45. The average error for the resistance was 1.2% and the maximum error was 4.1%. The resistance, side force, and yaw moment as a function of drift angle were compared against experimental values for the tanker ship KVLCC2, and two simplified ship geometries. The difference in the forces and moments between experiments and CFD was in general around or below 10%, with an average value around 5%.

#### 3.2.2. Aerodynamic mesh

An overview of the aerodynamic mesh is shown in Fig. 5. The wake downstream of the wings are refined within a box shape that covers the entire span length in the vertical direction. The wing tips and the trailing edge is refined one and two levels above the rest of the wing to better capture the geometry. All CFD simulations of the wingsails are done with a symmetry plane at the midspan to reduce the mesh size. The resolution shown in Fig. 5 corresponds to roughly 7 million cells for a single sail and 13–14 million cells for two sails.

The mesh resolution for the aerodynamic simulations was determined based on a convergence study with a single wing, at an angle of attack of 15° and a Reynolds number of 10 million. The smallest and largest mesh had 1.7 and 38 million cells respectively. The recommended practice from the International Towing Tank Conference (2017c) was used to estimate the error and uncertainty related to mesh resolution for both lift and drag. In short, least squares regression was used to fit polynomial models that estimated the error in the result as a function of mesh resolution. However, since the data showed some oscillatory behavior in the tested range for both the lift and drag, the final uncertainty was estimated based on the data range parameter. See (International Towing Tank Conference, 2017c) or (Kramer and Steen, 2022) for further explanation of the method. The mesh uncertainty at our chosen resolution was estimated to roughly 5.5% and 2.7% for the drag and lift coefficient respectively. This was for an angle of attack that is well below stall, but with a relatively high lift coefficient close to 1.0. The drag force on the wing is therefore dominated by lift-induced effects. The values of the drag coefficient, $C_D$, and lift coefficient, $C_L$, as a function of mesh resolution are shown in Fig. 6. Both coefficients are defined as the force on the sail divided by the dynamic pressure – equal to $0.5\,\rho\,U^2$, where $\rho$ is the density and $U$ the free stream velocity – and the planform area of the wing – equal to the chord multiplied by the span.

## 4. Hydrodynamic model

The resistance, side force, and yaw moment on the ship are first estimated with CFD simulations as a function of velocity, drift angle, rudder angle, and propeller thrust. The results are then used to tune route simulation models of the forces on the hull and rudder in calm water. Empirical models are used for the added resistance in waves and the propeller characteristics. The CFD based modelling of the ship is explained in Section 4.1 while the empirical models are outlined in section 4.2.

### 4.1. CFD-based models

#### 4.1.1. Coupling of CFD data and models

The models presented in this section are used to generalize the results

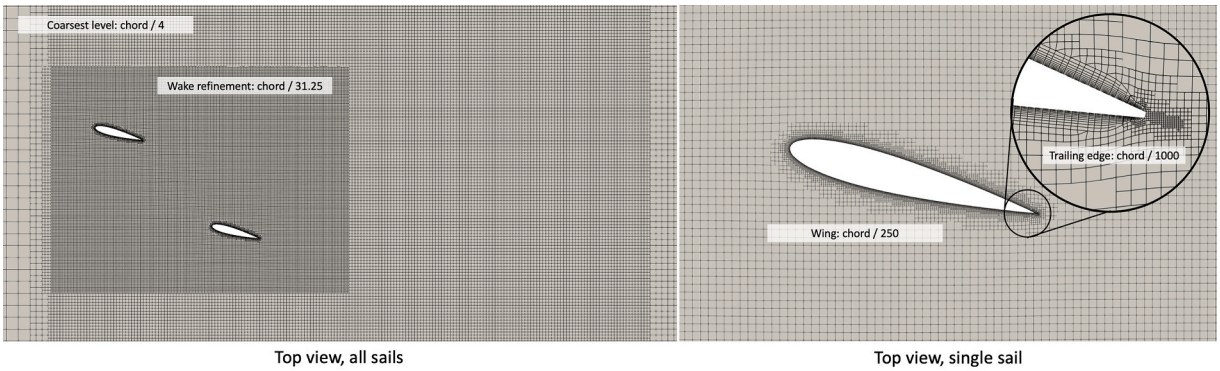


**Fig. 5.** Illustration of the aerodynamic mesh with values for the cell lengths at different regions.

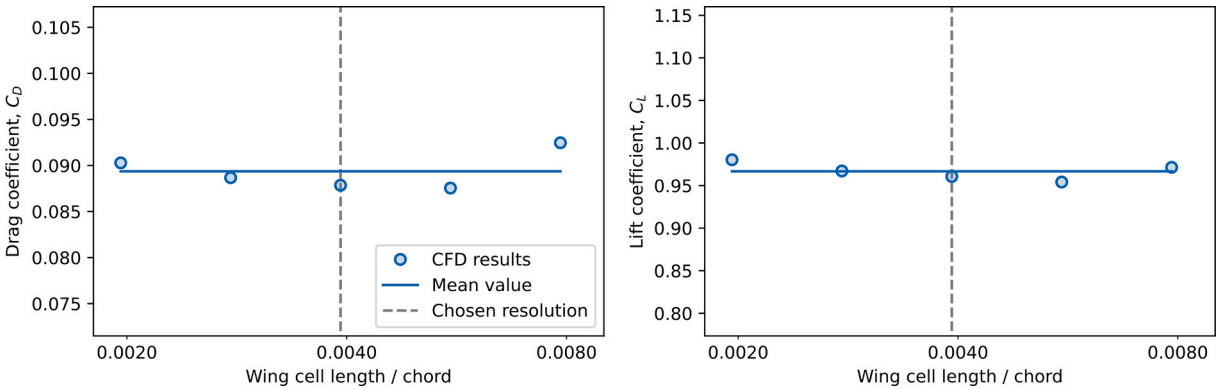


**Fig. 6.** Drag and lift coefficient for single wing as a function of mesh resolution.

from the CFD simulations to arbitrary ship states. The choice of modelling equations is based on two main goals: to reduce the number of CFD simulations to a level that is practical and to get models that are well behaved in numerical solvers, which are heavily used in the route simulations. The equations are therefore chosen based on a compromise between simplicity and accuracy. Each model is based on either existing ship maneuvering theory or theoretical lifting surface equations. In each equation, there are coefficients that are adjusted such that the model values and the CFD results matches as closely as possible. This is achieved with a least squares regression method. The models are implemented in the programming language Python, and we therefore use the curve fitting function from the optimization library in Scipy for this task (Virtanen and Al, 2020). The only difference between the tuning process of the different models is the objective function and input data that is given to the least squares regression method.

#### 4.1.2. Resistance on the hull in calm water and straight-ahead conditions

The calm water resistance on the hull, $R$, when no aerodynamic side force is applied to the ship is calculated from Equations (1) and (2). The frictional resistance coefficient, $C_F$, is found from the empirical friction line presented in (Eca and Hoekstra, 2008). The added friction due to surface roughness, $\Delta C_F$, is calculated with the empirical model in the "Performance Prediction Method" from ITTC (2017). The hull roughness, $k_s$, is set to 150 μm. The thrust-induced resistance is assumed to be linearly dependent on the propeller thrust, $T$, calculated with a thrust deduction factor, $t$. The other symbols in the equations are the wave resistance coefficient, $C_R$, the shape factor, $k$, the ship speed, $U_s$, and the wetted surface of the ship, $S$.

$$C_{T,S} = C_R(F_r) + (1+k)C_F(Re) + \Delta C_F(Re, k_s) \tag{1}$$

$$R(Fr, Re, T) = 0.5\rho S U_s^2 C_{T,S} + t\,T \tag{2}$$

The shape factor is adjusted so that the corrected friction matches the total resistance on the hull from double body simulations without any thrust from the propeller. The thrust deduction factor is adjusted based on two double body simulations with propeller thrust different than zero and assumed independent of ship speed. Two CFD simulations are executed for every design speed: one with free surface modelling and one without. The wave resistance is calculated as the difference in the resistance between the two. Spline interpolation is used to generalize the wave resistance model to Froude numbers not directly tested. The results from both CFD simulations and the tuned models can be seen in Fig. 7. The wave resistance is assumed to not be affected by the keel geometry and is therefore only calculated for the bare hull form. The shape factor for the bare hull and the hull with bilge keels is estimated to 0.100 and 0.142 respectively. The thrust deduction factor is almost identical between the two design configurations with a value of approximately 0.10. The effect of the high aspect-ratio keel is not shown in the plots below, as this component is treated with a separate model explained in Section 4.1.4.

#### 4.1.3. Hull and rudder under the influence of sail forces

The forces and moments on the ship as a function of drift angle, rudder angle, and propeller thrust are estimated based on a slightly modified version of the MMG maneuvering model (Yasukawa and Yoshimura, 2015). This modelling approach was one of the main topics in our recently published article (Kramer and Steen, 2022), where we explored both the tuning processes and the accuracy. The explanation in this article is therefore kept brief. Most of the original formulations from the standard MMG model is kept. For route simulations, all terms related

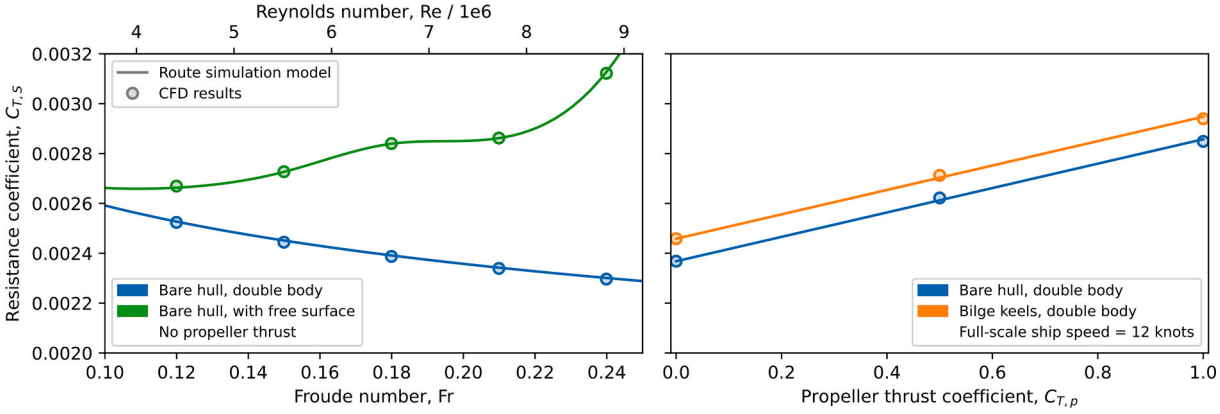


**Fig. 7.** Calm water straight ahead resistance of the hull in model scale 1:4. The plot to the left shows the wave resistance and the viscous resistance without bilge keels. The plot to the right shows how the resistance varies as a function of propeller thrust. The values on the y-axis are the same for both plots.

to unsteady effects are neglected, such as the yaw rate and inertia. The model includes interaction effects between the rudder and the hull through a polynomial model for the flow straightening in the wake and the induced lift on the hull from the rudder. The effect of the propeller is modeled with a simple expression based on actuator disk theory. Different from the standard MMG model, we calculate the lift and drag force on the rudder based on classical lifting line equations, rather than the "normal force" approximation. This change was done to improve the accuracy of the rudder resistance, based on results presented in (Kramer and Steen, 2022). The lift and drag act normal and parallel to the effective rudder velocity vector estimated from the MMG model. The rudder drag is scaled to different Reynolds numbers based on the same empirical friction line used for the hull resistance multiplied with a rudder shape factor, $k_r$. The expressions are shown in equations (3) and (4), where $C_L$ and $C_D$ are the lift- and drag-coefficient respectively. The symbol $\delta_e$ is used for the angle of attack of the rudder which is corrected for flow straightening effects according to the MMG model. The symbol $\lambda$ is used for the geometrical aspect-ratio, while $e_L$ and $e_D$ are correction factors used to tune the model to CFD results.

$$C_L = \frac{2\pi\delta_e}{1+\frac{2}{\lambda\, e_L}} \tag{3}$$

$$C_D = 2(1+\,k_r)\,C_F(Re) + \frac{C_L^2}{\pi\,\lambda\,e_D} \tag{4}$$

The coefficients in the model are adjusted based on CFD results from double body simulations with both the rudder and the hull together. The simulations are done in model scale 1:4, and only for a single velocity – corresponding to 12 knots full scale. The CFD results used in the tuning procedure consist of a static drift test with zero propeller loading, and three static rudder tests with propeller thrust loading coefficients equal to 0.0, 0.5 and 1.0. The thrust loading coefficient in the route simulations was between these values most of the time. The rudder model, including the rudder-induced forces on the hull, was found to be almost independent of the keels. We therefore limit the presentation of the rudder forces to one ship geometry to reduce clutter in the plots.

Two differences in the tuning procedure were implemented for this paper relative to (Kramer and Steen, 2022). First, the process for finding the wake factor in the MMG model is somewhat ambiguous. We have previously used the average velocity field at the rudder location from a CFD simulation without the rudder present. In this study, the wake factor is adjusted so that the difference in the effective aspect-ratio for the lift and drag is minimized. This is a slightly more practical approach. Second, the standard MMG model assume that all model coefficients are independent of the propeller thrust. This was also found to work well for the case study in (Kramer and Steen, 2022). However, for the ship in this paper, both the rudder shape factor in equation (4) and the coefficients for the rudder-induced hull forces varied somewhat as a function of the thrust loading coefficient. We therefore used linear interpolation on the coefficient data to calculate the values for arbitrary thrust loading coefficients. Although this illustrates an inaccuracy in the assumptions in the MMG model, it is a relatively minor issue. Both the rudder drag at zero rudder angle and the rudder-induced hull forces are small relative to the other parts of the force model.

The effect of heel on the drift induced forces are neglected which is also a common simplification for maneuvering simulations. This choice was based on our previous work (Kramer and Steen, 2022) where we investigated the effect of heel on the drift-induced forces on a ship similar to the one in this study. In short, we found that heel angles mainly affect the drift-induced forces in cases with large cross-flow drag – as a consequence of large drift angles – while the effect was found to be small for the circulatory lift on the hull. The coupling effects between heel angles and drift angles could be important for many sailing ships, but we allowed for this simplification in this case study as both the drift angles and the heel angles are relatively small. This will be shown in the data from the route simulations in Section 7.2. We also used a slightly simplified approach for the relationship between the rudder and propeller. Due to the rotational motion of the propeller jet, there can be differences in the rudder model for positive and negative drift angles (Yasukawa and Yoshimura, 2015). This effect was neglected for the current study to reduce the number of required CFD simulations.

Fig. 8 shows the match between the CFD results and the tuned model for the hull forces as a function of drift angle, rudder angle and propeller thrust. It shows that the bilge keels increase both the lift and lift-induced resistance relative to the bare hull, while the yaw moment is not much affected. The rudder-induced hull force was found to be 27%, 22% and 18% of the rudder sway force for thrust loading coefficients 0.0, 0.5 and 1.0 respectively. Fig. 9 shows the match between CFD and the tuned models for the rudder forces. The data used for tuning the rudder model for different drift angles were limited to 3 and 6°, as this gave a better match between the model and the CFD results at low drift angles. As will be shown in Section 7.1.1, the drift angle during the route simulations was generally below 6°. The effective aspect-ratio for the rudder was found to be 0.93 times the geometrical aspect-ratio. The value of the rudder shape factor was 1.5, 1.8 and 0.6 for increasing thrust loading coefficients. The wake factor at the rudder was estimated to approximately 0.19 for both hull forms. The flow straightening from the hull with bilge keels is seen to be larger than for the bare hull. At a given drift angle, the effective rudder angle with bilge keels is estimated to be around half the value of the bare hull. The consequence of these differences for the overall resistance of wind-powered vessel will be explored further in Section 7.

#### 4.1.4. High aspect-ratio keel model

The high aspect-ratio keel is modeled with the same general expressions as the rudder. However, as the keel is placed underneath the hull, the model for the effective velocity is simplified. The effective angle of attack is set equal to the drift angle for a static keel and by adding the drift angle with the imposed keel angle in the case of a dynamic keel. The ships forward velocity without any correction for a wake is used to compute forces from the lift and drag coefficients. The correction factors for the aspect-ratio and the shape factor for the keel is estimated from CFD simulations of the keel, hull, and rudder together, where both the drift angle and the dynamic keel angle are varied. A comparison between the forces predicted by the tuned model and the raw CFD results are shown in Fig. 10. The effective aspect-ratio of the keel was estimated to be 1.5 times the geometrical aspect-ratio for both the lift and drag. The expressions from the MMG maneuvering model computes an additional sway force and yaw moment on the hull as a function of the rudder force. A similar behavior was observed for the interaction between the keel and the hull. At a drift angle equal to zero degrees there was a sway force on the hull that was roughly 25% of the sway force on the keel. The induced yaw moment and surge force on the hull was negligible. The rudder also experienced a small lift force when the keel angle was varied, corresponding to approximately 10% of the lift on the keel. This indicates that the rudder experiences some lift-induced velocities due to the keel. However, we neglected this effect for simplicity.

### 4.2. Empirical models

#### 4.2.1. Added resistance in waves

The added resistance in waves is calculated using the empirical model known as SNNM (Liu and Papanikolao, 2020). The side force and yaw moment from the waves are neglected for simplicity. As an example of the output from the model, the calculated response amplitude operator (RAO) of the added resistance in waves for our case study ship is shown in Fig. 11. The data is shown for different wave directions and wave lengths, labeled $\lambda_{wave}$. The RAO can be combined with wave spectrum data to compute the mean added resistance, $\overline{R}_{AW}$, in short crested irregular waves according to equation (5). In this equation, $S$ is the wave spectrum as a function of wave direction, $\alpha$, and wave

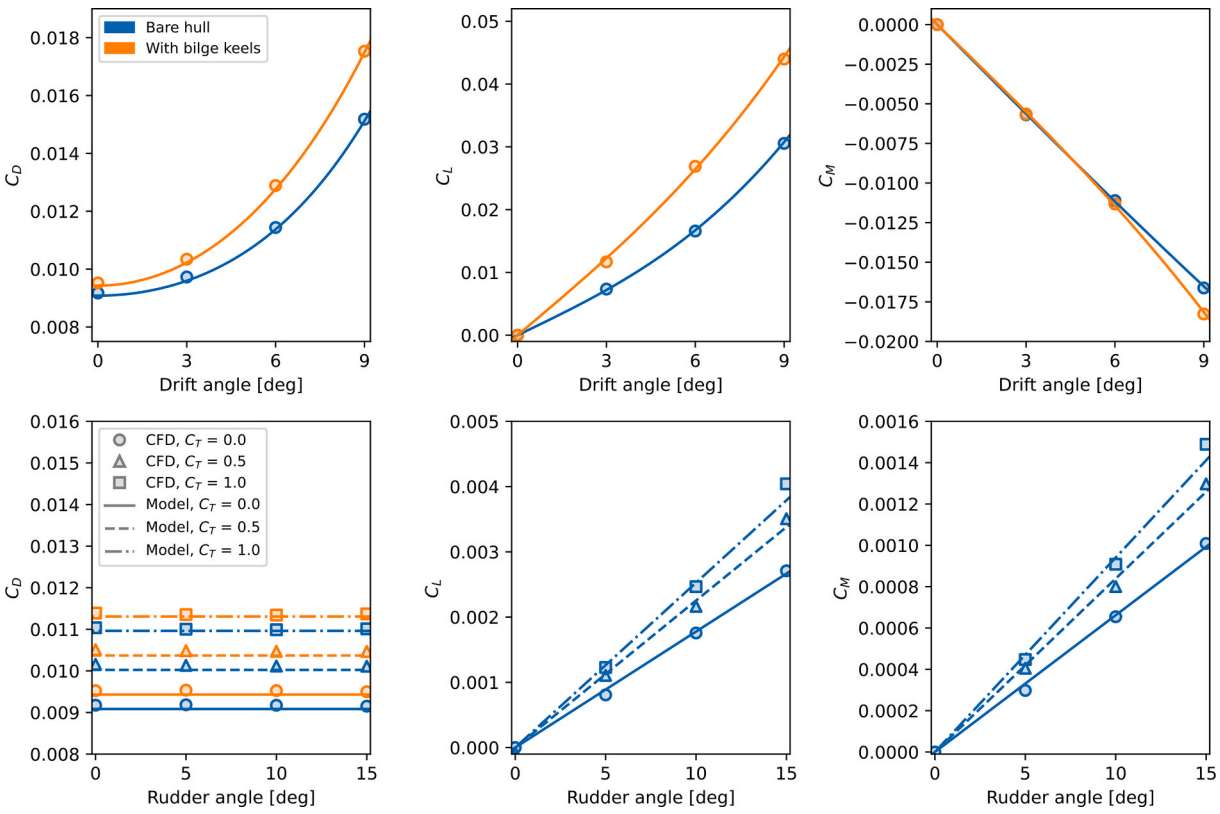


**Fig. 8.** CFD results and tuned models for the hull. The coefficients for drag, $C_D$, lift, $C_L$, and yaw moment, $C_M$, are made non-dimensional by the dynamic pressure based on the ship speed and the underwater hull lateral area calculated as the ship length multiplied by the depth. The yaw moment is measured relative to the midship location, and the coefficient is divided by the ship length in addition to the area.

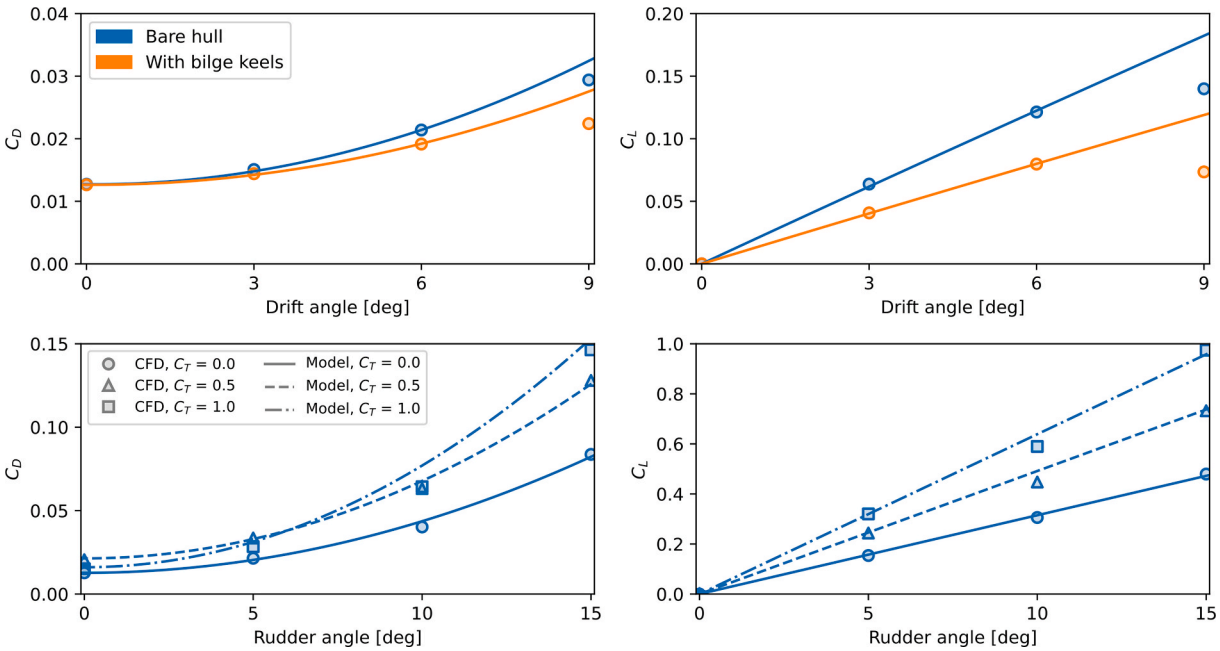


**Fig. 9.** CFD results and tuned models for the rudder as a function of drift angle and rudder angle. The coefficients for the rudder drag, $C_{D,}$ and lift, $C_{L,}$ are made non-dimensional by the dynamic pressure based on the ship speed and the rudder planform area.

frequency, $\omega$. The wave resistance for a single harmonic wave is labeled $R_{AW}$, computed using the SNNM method. The ship speed is labeled $U_s$, and the wave amplitude $\zeta_A$.

$$\overline{R}_{AW} = 2\int_0^{2\pi}\int_0^{\infty} \frac{R_{AW}(\zeta_A,\ \omega, \alpha, U_s)}{\zeta_A^2} S(\omega,\alpha)\, d\omega d\alpha \tag{5}$$

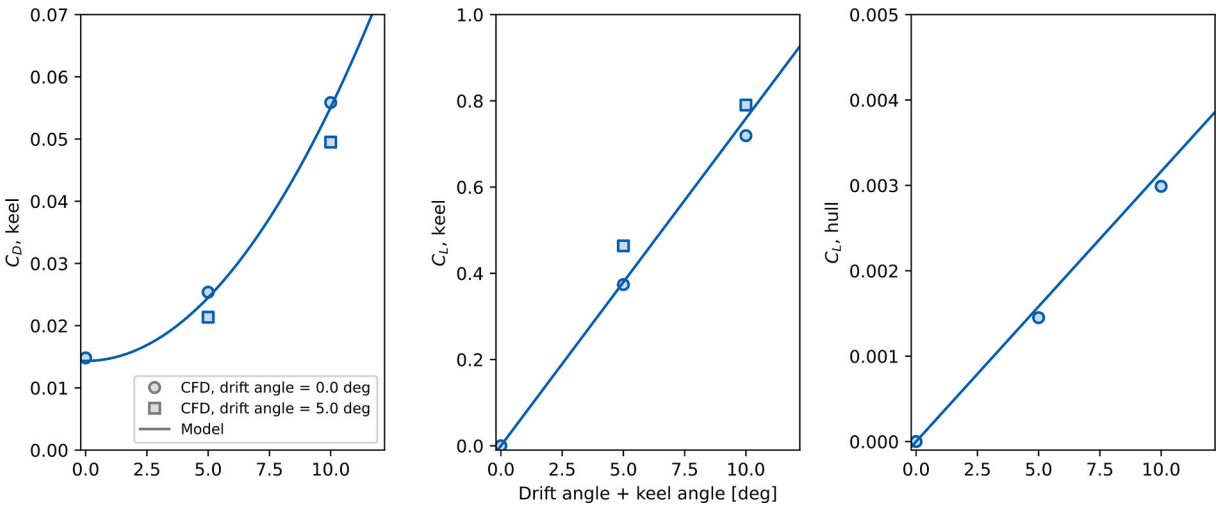


**Fig. 10.** Keel forces as a function of drift and keel angle. The force coefficients for the keel are made non-dimensional by the dynamic pressure and the keel planform area. The hull lift coefficient is calculated based on the underwater lateral area.

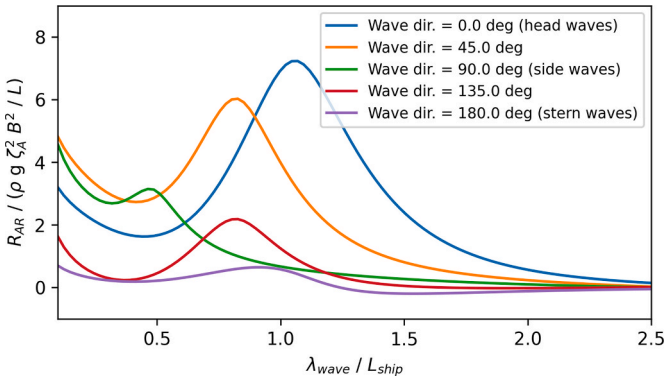


**Fig. 11.** RAO for the added resistance in waves from the empirical model as a function of wavelength and wave direction. The ship speed used in the generation of the plot was 12 knots.

The integration of equation (5) is done numerically using the trapezoidal method. The wave frequencies are limited to wavelengths between 0.1 and 3 times the ship length, with 21 discrete steps. The integration of wave directions has a step size of 5°. A two-dimensional wave spectrum is created from the wave data used in the route simulation, which is further presented in Section 6.2. The input variables are the significant wave height, $H_s$, the peak frequency, $\omega_p$, the mean direction, $\theta_0$, and the directional spreading, $\sigma$. A Pierson-Moskowitz spectrum (DNV, 2014) is used in the frequency domain and a Gaussian spectrum (International Towing Tank Conference, 2017b) in the directional domain. The expressions are shown in equations (6)–(8).

$$S(\omega,\theta) = F(\omega)\cdot D(\theta) \tag{6}$$

$$F(\omega) = \frac{5\, H_s^2 \omega_p^4}{16\, \omega^5} Exp\left(-\frac{5\, \omega_p^4}{4\, \omega^4}\right) \tag{7}$$

$$D(\theta) = \frac{1}{\sqrt{2\pi\sigma}} Exp\left(-\frac{(\theta-\theta_0)^2}{2\sigma^2}\right) \tag{8}$$

#### 4.2.2. Propeller model

The empirical polynomials for the Wageningen B-series are used as a model for the propeller open water characteristics (Oosterveld and Oossanen, 1975). The pitch ratio was set to 1.2, the expanded blade area ratio to 0.8, and number of blades to 4. The open water characteristics can be seen in Fig. 31 in Section 7.2 together with statistics of the simulated advance ratios for the case study ship. Originally, we considered introducing a variable pitch propeller in the modelling framework. However, this plan was dropped when we discovered that the required power to the propeller at zero thrust is small, even with fixed pitch. As an example, at 12 knots speed and zero thrust, the propeller only requires around 3% of the necessary power without sails. The thrust is assumed to always point in the axial direction of the ship and sway forces are neglected. The required revolutions for given thrust and speed is found by using a numerical solver based on Newton's method. The velocity experienced by the propeller, $U_p$, was calculated from the ship speed with a constant wake factor, $w_p$, and a simplified correction for the drift angle based on the suggested expression from (Amini et al., 2012). The expression is shown in equation (9).

$$U_p = U_s(1-w_p)\cos\beta \tag{9}$$

The wake factor at the propeller location is found from the velocity field from a CFD simulation of the hull alone, shown in Fig. 12. The relative wake factor is assumed constant for different ship velocities.

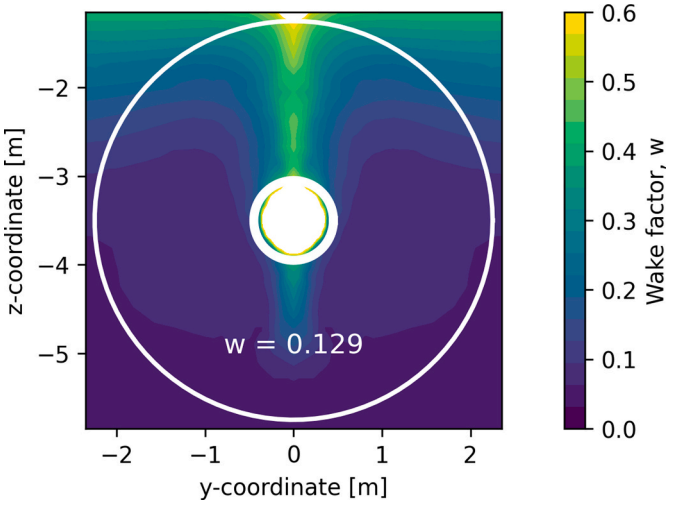


**Fig. 12.** Wake field at the propeller location in CFD simulations at model scale 1:4.

## 5. Aerodynamic model

The sails are simulated with a discrete lifting line method which also include simplified expression for the forces on the sails for angles of attack above stall. The ship deck is assumed to be relatively flat and without significant obstacles. All effects related to the superstructure is therefore neglected for simplicity. First, an overview of our implementation of the aerodynamic model is given in section 5.1. Then, the lifting line is compared with CFD simulations in section 5.2. Finally, the forces from the aerodynamic model as a function of apparent wind direction is presented in Section 5.3.

### 5.1. Implementation

#### 5.1.1. Lifting line

The discrete lifting model is built on the same fundamental principle as the classical lifting line method developed independently by Prandtl (1918) and Lanchester (1907). However, it is extended to handle non-planar wings, several wings in the same simulation, and non-linear relationship between lift and angle of attack. We have previously explored the accuracy of this method when modelling non-planar wing shapes in (Kramer et al., 2018). The current paper shows some further validation results for the interaction effects between two wings. Other papers with similar discrete lifting line methods can be found in (Hunsaker, 2011), (Phillips and Snyder, 2000) and (Duport et al., 2017). An overview of the geometry of the lifting line method is shown in Fig. 13. Each sail in the simulation is built up by 10 horseshoe vortices with different vortex strength along the span of the wing. The resolution was determined based on a compromise between computational time and accuracy. The lift and drag with 10 horseshoe vortices on a single wing at an angle of attack of 10° only differed from a test with 100 horseshoe vortices by roughly 4%. The bound vortices are placed at the quarter chord, while the free vortices are oriented such that they point in the direction of the free stream velocity. At the middle of each bound vortex, there is a control point where induced velocities are computed. The ocean surface is modeled as a symmetry plane. The induced velocity from a vortex segment is linearly dependent on the line geometry and the strength. The full set of equations for calculating the induced velocities from vortex lines are presented in both (Katz and Plotkin, 2001) and (Maskew, 1987).

The lift force on each segment is defined as the force component acting normal to both the incoming velocity and the vortex line. It can be calculated in two ways. First, Kutta-Juokowski's law states that the lift on the bound vortex is proportional to the vortex strength and the velocity magnitude. Second, the lift can be calculated from the two-dimensional lift-coefficient of the foil profile as a function of the effective angle of attack, which is further explained in Section 5.1.2. The vortex strength can be found by requiring that both expressions give the same value. There are several ways to solve this system. For angles of attack below stall, it is possible to use local linearization to solve the system very rapidly, as we outline in (Kramer et al., 2018). Although the method can handle some non-linear effects, it tends to become unstable for angles of attack close to stall. A slower but more robust method is therefore used in this case study. This solver is a direct implementation of the method described in (Anderson, 1991), chapter 5. It starts by setting the strength of each vortex segment based on the geometric angle of attack and the foil profile model. Then, the induced velocities with the current vortex strength are calculated, which gives a new estimation of the effective angle of attack at each control point. The vortex strength is updated based on the new estimation, but with significant numerical damping to make the solver stable. This loop continues until the vortex strength converges. See (Anderson, 1991) for more.

#### 5.1.2. Foil profile model

A requirement for the method is a function that calculates the two-dimensional lift and drag on each control point as a function of the effective angle of attack. From the perspective of the lifting line, the source of this data can be from both simulations and experiments. However, the optimal angle of attack for the wingsails is very close to stall for most wind directions. As for instance shown in (Rumsey et al., 2019) and (Blount and Protell, 2021), this is a region where RANS CFD simulations often contain large uncertainties. We therefore used the experimental data from (Sheldahl and Klimas, 1981) for the current case study. The report presents lift and drag coefficients for several symmetrical foil sections for a range of angles of attack between 0 and 180°. The data for the foil profile NACA 0015 and Reynolds number equal to 10 million is used, which corresponds to an apparent wind speed of roughly 9 m/s for the dimensions of the sails in this study. The exact stall angle will depend on both Reynolds number and other environmental factors, such as the turbulence level in the atmosphere. For simplicity, we assume that the foil profile model is independent of the weather conditions. Spline interpolation is used to generalize the model to arbitrary angles of attack.

#### 5.1.3. Three-dimensional corrections to the post-stall drag coefficient

The three-dimensional effects on the forces acting on the sail can be divided in two: the effects of lift-induced velocities and the reduction to the viscous drag due to finite span effects on the separated flow. The first

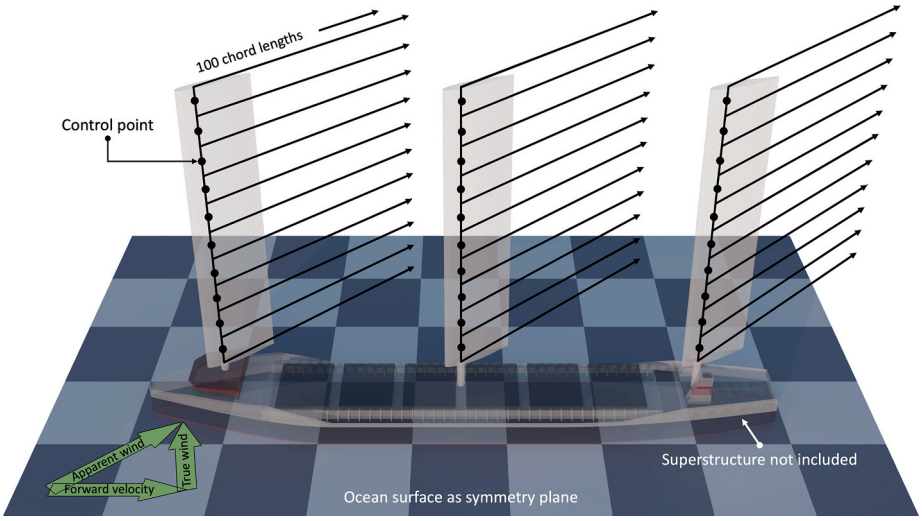


**Fig. 13.** Lifting line geometry.

effect is directly captured by the lifting line method. To capture the second effect, the drag from the two-dimensional foil profile model is multiplied with a correction factor for large angles of attack. The correction is based on values found in (DNV, 2014). For a rectangular surface with aspect-ratio of 4 – the value for the sails in this case study – the three-dimensional drag coefficient is reduced to roughly 65% of the two-dimensional value. The reduction should only be applied to the drag coefficient when the flow is separated, and not when the sails are operated as lifting surfaces. The correction is therefore gradually introduced by linearly decreasing it from 1 to 0.65 for effective angles of attack between 20 and 30°. An overview of both two-dimensional and three-dimensional force coefficients are presented in Fig. 14, which shows the effect of both lift-induced velocities and the simplified model for finite span effects on the drag.

#### 5.1.4. Viscous wake

In addition to the lift-induced velocities from the horseshoe vortices, there are also viscous interaction effects between the sails in the simulation. A sail downwind of another sail will experience a reduction in the incoming velocity due to the viscous wake from the upwind sail. This is mainly an issue when the sails are operated with angles of attack above stall, which causes highly separated flow. To model this effect, we use the same procedure as outlined in (Bordogna, 2020). The reduction in velocity behind a sail is calculated according to a simplified wake model, shown in equations (10) and (11). The input to the method is the free stream velocity, $U_\infty$, the integrated viscous drag coefficient on the sails, $C_{D,v}$, and the projected width of the sail relative to the incoming velocity, $d_w$. This velocity reduction is calculated iteratively in the lifting line method, along with solving the vortex strength. For each iteration, the viscous wake is estimated from the drag coefficients and the average velocity in the last iteration. The reduction in the velocity only happens directly downwind from each sail. The coordinates in the equation, $x$ and $y$, refers to downwind direction – positive x – and normal to the downwind direction respectively. The effect of this model can be seen Fig. 14. The thrust is significantly reduced in downwind conditions when several sails are simulated together. However, for most wind directions, the viscous wake model has little to no effect on the forces. The report in (Bordogna, 2020) contains further discussion and experimental validation of this model for both rigid sails and rotor sails.

$$U_{viscous} = U_\infty \left(1 - 0.98\left[\frac{x}{C_D\, d_w}\right]^{-0.5}\left[1 - \left(\frac{2y}{b}\right)^{1.5}\right]^2\right) \tag{10}$$

$$b = 1.14\left(C_{D,v}\, d_w\, x\right)^{0.5} \tag{11}$$

#### 5.1.5. Atmospheric boundary layer

The free stream velocity in the aerodynamic model is a combination of the ships forward velocity and the wind velocity. For a real ship, the wind speed and direction will vary as a function of the height above the sea due to the atmospheric boundary layer. Although the lifting line model can handle this variation, we chose to neglect it to simplify the control policy of the sails – explained further in Section 5.3.1. A simplified expression for the vertical variation in the wind speed due to the atmospheric boundary layer effects is shown in equation (12). The variable $U_{10}$ is the wind speed at 10 m height, $z$ is the distance above the ocean surface, and $z_0$ is a parameter representing the effective surface roughness. The report in (DNV, 2014) states that the value of the surface roughness will typically vary between 0.0001 for calm water conditions to 0.01 for weather conditions with significant waves. We have used a constant value of 0.0002. The input to the lifting model is the height averaged value of the wind speed, based on equation (12).

$$U_W(z) = U_{10}\frac{\log\left(\frac{z}{z_0}\right)}{\log\left(\frac{10}{z_0}\right)} \tag{12}$$

### 5.2. Comparison between lifting line and CFD

#### 5.2.1. Single sail

Fig. 14 shows the lift and drag coefficient for a single sail and on the 2D foil profile model for different angles of attack. The foil profile data is the experimental data from (Sheldahl and Klimas, 1981), while the three-dimensional values are computed both with the lifting line model and with CFD simulations. The purpose of the comparison is primarily to validate the lift-induced effects on the forces calculated by the lifting line method. We have therefore only tested angles of attack below stall. The grey dashed line in the figure shows the maximum angle of attack that is used when a single sail operates in “lift-mode”, explained further

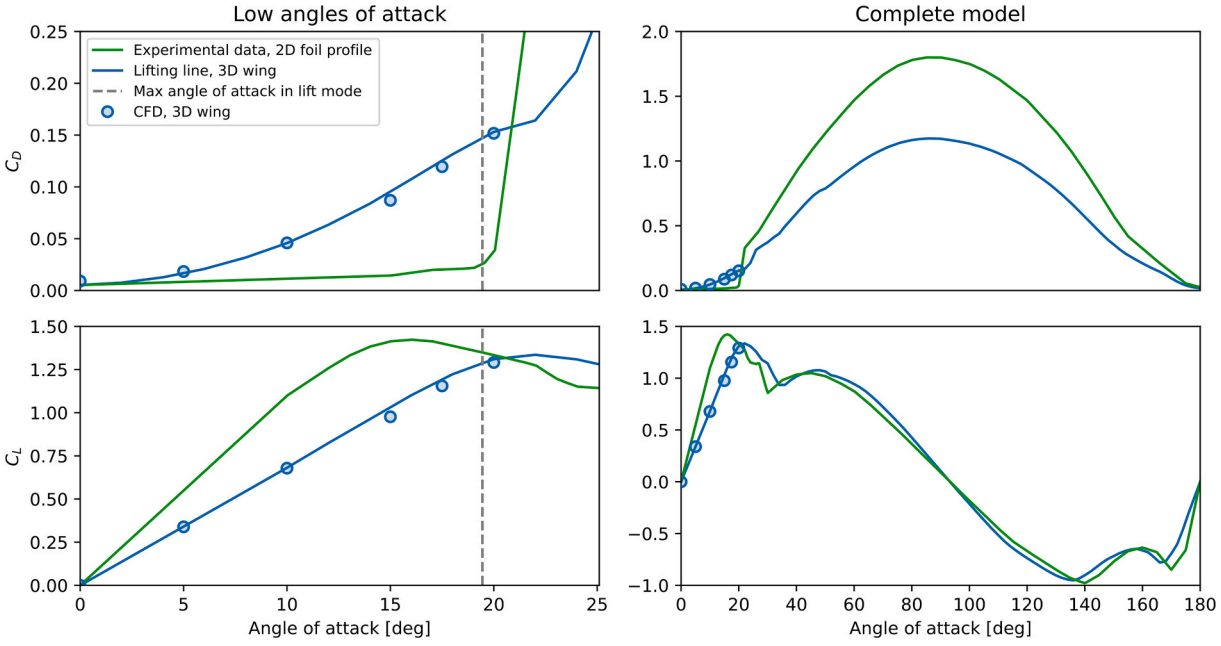


**Fig. 14.** Comparison between the experimental two-dimensional foil profile model, the lifting line method based on the foil profile model and CFD simulations for a single three-dimensional sail. The Reynolds number is 10 million, both for the experimental data and the CFD simulations.

in Section 5.3.1. In short, the sails are mostly operated below this limit in the route simulations. The sails were simulated with a symmetry at the midspan to reduce the mesh size in the validation test. This is equivalent to removing the ocean symmetry plane shown in Fig. 13. The effective aspect-ratio is therefore slightly lower in the validation test than in the sail model in the route simulations. This will increase the lift-induced velocities and is therefore considered a more challenging validation case for the lifting line model.

#### 5.2.2. Interaction effects

Fig. 15 shows a comparison of the interaction effects predicted by the lifting line model and CFD simulations. Running CFD simulations of multiple wings together can lead to large meshes. This validation test was therefore adjusted somewhat relative to the sail model used in the route simulation to reduce the computational time. First, although the test is done with two sails, the space between the sails was adjusted to match the configuration with three sails. That is, the space between the sails is set to 45 m, and not 90 m as would be the case for two sails in the route simulations. This was done to increase the interaction effects in the validation test – to roughly correspond to a case with three sails – without having to include more sail geometry in the CFD simulations. Second, the sails were simulated with a symmetry plane at the midspan – in the same way as for the single sail validation test in Section 5.2.1. The angle of attack of the sails where set to 15°, while the apparent wind angle was varied. We then measured the forces acting on each individual sail. Thrust is defined as the force pushing along the ship's center line, while the side force is the force normal to the thrust. The forces are made non-dimensional by dividing them by the dynamic pressure and the planform sail area. Both the CFD simulations and the lifting line model show clear interaction effects, as both the thrust and the side force vary between the two sails. The max difference between the lifting line model and the CFD simulations is approximately 5.9% for the side force on the stern sail at an apparent wind direction of 20°. The error in the total side force on both sails for the same case is only 2.0%.

### 5.3. Aerodynamic forces

#### 5.3.1. Maximizing thrust

The angle of attack as a function of weather conditions in the route simulations is set based on a control policy. The full policy also depends on the hydrodynamic response of the ship – which will be further explained in Section 6.1 – but the starting point is the angle of attack that maximize the thrust from the sails. Due to the simplifications introduced in the aerodynamic modelling, the optimal angle is only dependent on the apparent wind direction and independent of the apparent speed. We first assume that there are two distinct modes of operation for the sail: "lift-mode" – where the angle of attack is below stall – and "drag-mode" – with angles of attack above stall.

The optimal angle of attack in lift mode is found using a line search method from the SciPy library (Virtanen and Al, 2020). To make sure the optimization results stay within the pre-stalled part of the model, the effective angle of attack halfway up the sails is limited to 16°. This is achieved by adding quadratic penalty to the objective function if the limit is exceeded. The reason for this limit was to stabilize the optimization and avoid spikes in the results when lift-mode and drag-mode provide similar values of thrust. The effective angle of attack is measured by adding the induced angles of attack from the lifting line simulation to the geometrical angle of attack. In drag mode, the sails are set to an orientation normal to the ship center line. The limit for when the policy should switch from lift-mode to drag-mode is set manually. For apparent wind directions larger than approximately 130°, drag-mode was found to give the best results. The resulting control policy for three sails is shown in Fig. 16, as an example. The figure also illustrates the interaction effects in the control policy for multiple sails; when one sail is placed close to the wake from another, the angle of attack is increased on the downstream sail to adjust for the induced angle of attack from the upstream sail.

#### 5.3.2. Resulting forces

The resulting thrust and side force when using this operational policy is shown in Fig. 17 for varying number of sails. The forces are made non-dimensional by the total sail area and the dynamic pressure based on the apparent wind speed. As the sails are optimized including interaction effects, the non-dimensional values for the forces are not very dependent on the number of sails. A notable exception is for downwind sailing, where the viscous wake has a large effect. Large side forces from the sails are mainly an issue for apparent wind angles less than 60°. However, the smaller apparent wind directions are more likely than the larger values due to the forward velocity of the ship, as will be shown in Section 6.2.

## 6. Route simulation

The route simulation calculates statistics for all variables in the complete ship model for the weather conditions on the route. The most important results are the estimated fuel savings for the ship due to wind-power, the magnitude of the different resistance components in the model, and the magnitude of the ship response due to the sail forces – i.e., drift angle, rudder angle, heel angle and thrust from the propeller. Two major simplifications are made when running the route simulation. First, we only calculate the steady-state conditions of the ship and neglect all time varying dynamics. This includes maneuvering conditions, short variations in wind speed such as wind gusts, and wave-induced ship motions. Second, the logistics of the ship is not analyzed. Every geographical point and time instance on the route is therefore assumed to be equally likely. Using both simplifications means that we can represent the case study route as a dataset with independent

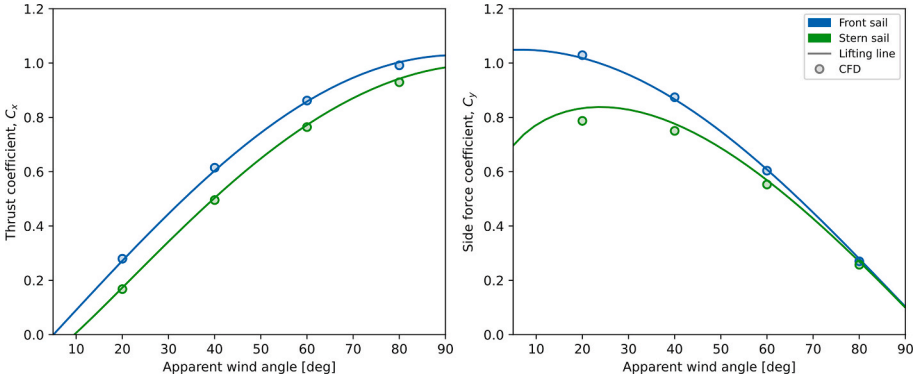


**Fig. 15.** Comparison of the interaction effects between two wing sails calculated by the lifting line method and with CFD. The geometric angle of attack on the sails where set to 15°, and the space between the sails was 45 m.

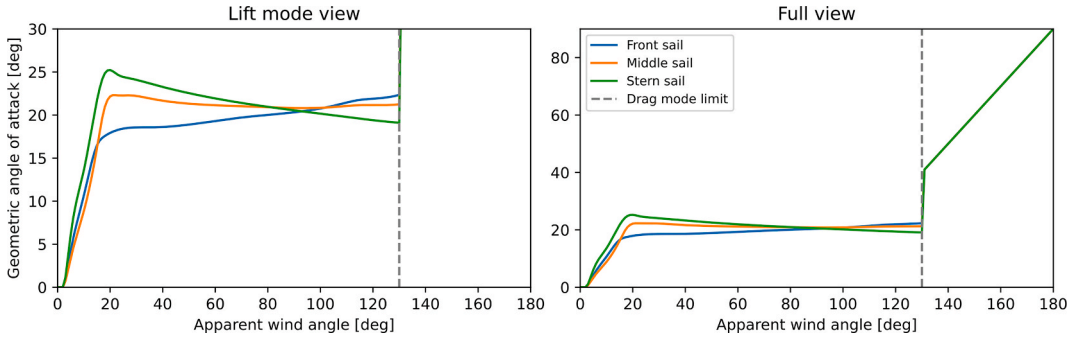


**Fig. 16.** Control policy for three sails showing the geometric angle of attack that gives the maximum thrust as a function of apparent wind angle.

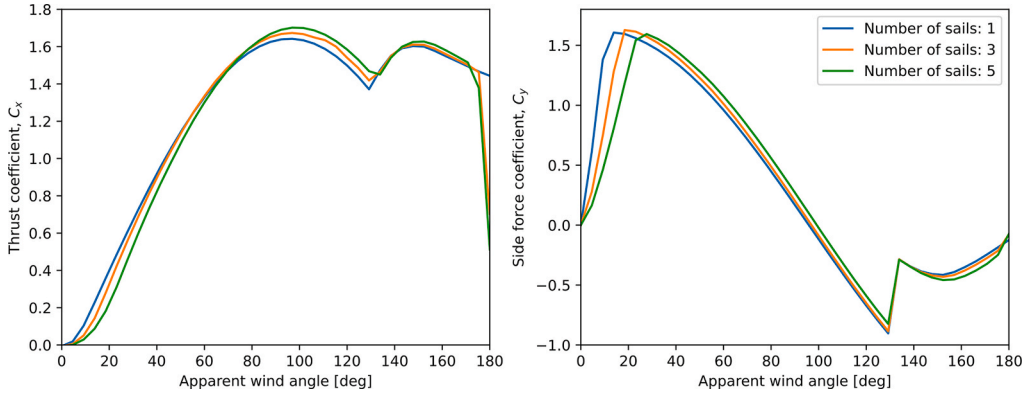


**Fig. 17.** Sail forces predicted by the lifting line model and the max thrust policy. The forces are made non-dimensional by the dynamic pressure of the apparent wind and the total sail area.

weather conditions. The aerodynamic forces and moments are computed from wind data, and the hydrodynamic forces are computed from the sail-forces and wave data on the route. Fig. 18 gives an overview of how the input data is used together with the different models.

### 6.1. Control algorithms and solvers

#### 6.1.1. Hydrodynamic solver

The variables in the hydrodynamic model must be adjusted to balance the aerodynamic forces and moments from the sails. The drift angle, rudder angle, and thrust from the propeller is found in a coupled analysis with the sail thrust, side force and yaw moment as input. This is done with a numerical non-linear solver from the Scipy library (Virtanen and Al, 2020), which is an implementation of the Newton method. The required heel angle of the ship is solved separately from the other ship states based on the hydrostatic model of the hull and the dynamic heel moment from the appendages. Most of the time, the ship was operating at the design speed. However, in a few cases with particularly high added resistance in waves, the speed was reduced so that the required power never exceeded the maximum power installed in the ship. This

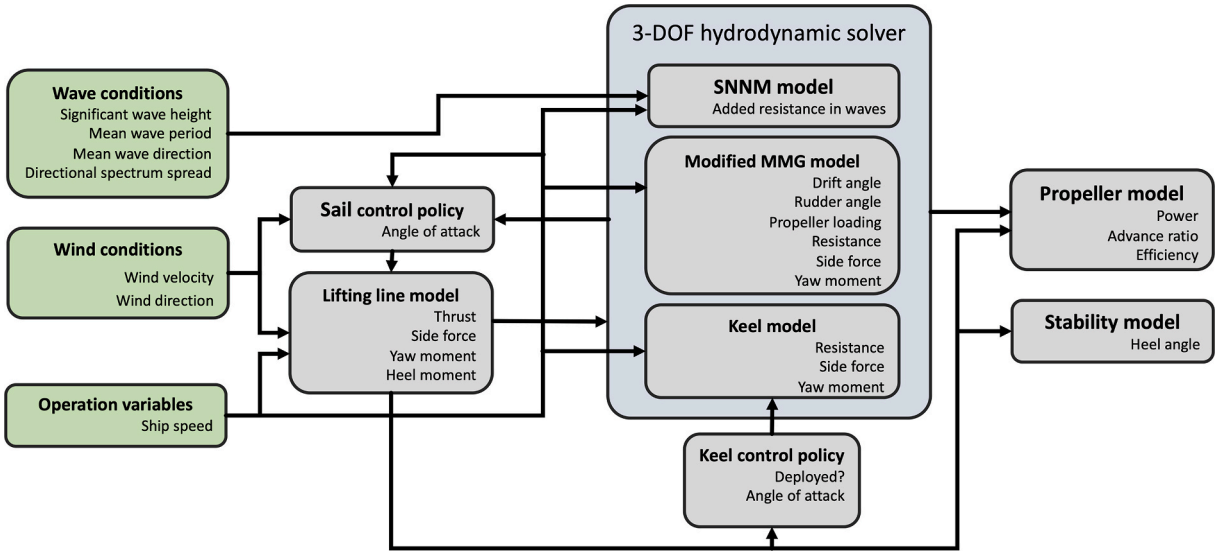


**Fig. 18.** Overview of the route simulation algorithm for a given weather condition and ship speed.

was done using an outer loop that iteratively reduces the velocity with 0.5 knots step size until the required power is less than the max power for the ship.

#### 6.1.2. Sail control algorithm

Two control algorithms for the sails were evaluated in this project. The first algorithm maximizes the thrust for any given weather condition – as explained in Section 5.3.1 – but with limits based on the forces on the sails and response of the ship. If any limit is exceeded, the angle of attack of the sails is reduced. The limits are as follows:

- The heel angle is limited to a maximum value of 10° to ensure sufficient ship stability. There are some ambiguities in exactly what this limit should be for a wind-powered cargo ship, but one possible guideline is class rules for stability. For instance, the rules in (DNV-GL, 2016) recommends that the maximum heel angle due to steady wind loads should be maximum 16° or 80% of the angle of deck immersion. As another comparison, the route simulations presented in (Tillig and Ringsberg, 2020) use 8° as a maximum heel limit.
- The rudder lift-coefficient is limited to a maximum value of 1.0. This is a convenient way to set a suitable limit for rudders with different effective aspect-ratios. A high aspect-ratio rudder will stall at a lower geometrical angle than a low aspect-ratio rudder, but the magnitude of the lift-coefficient is likely to be similar. The lift-coefficient is calculated based on the effective rudder velocity from the MMG model, which includes interaction from both the hull and the propeller. As a comparison (Tillig and Ringsberg, 2020), uses 10° as a limit on the geometrical rudder angle in their route simulations. This would correspond to a limit on the lift-coefficient of approximately 0.5 for our case study.
- The side force on the sails is limited independently of the ship response. The purpose is to be able to adjust the operation of the sails independently of the ship configuration. We set the limit using a side force coefficient made non-dimensional by the dynamic pressure based on the ship speed and underwater planform area. The allowable side force from the sails is therefore higher for higher ship speeds. The largest value for this side force coefficient is set to 0.04, which corresponds a side force that is between 2.9 and 3.0 times the calm water straight ahead resistance, depending on the ship speed. We also explore the effect of varying the value of this limit in Section 7.2.4
- The thrust from the sails is limited to the total resistance at the target speed.

These limits are implemented in the route simulation framework by multiplying the angle of attack from the sail policy presented in Section 5.3.1 with a reduction factor whenever the limit is exceeded. The same reduction factor is used for all sails in cases with multiple sails. The necessary value of the reduction factor is found by using the same type of numerical solver as outlined in Section 6.1.1. The objective function for the solver is the actual value for the variable that exceeds a limit minus the maximum value. Each limit is checked and enforced one by one, starting with the side force limit, then the heel limit, the rudder limit and finally the thrust limit.

The second control algorithm includes hydrodynamic effects on the resistance and power delivered to the propeller when adjusting the sails. The algorithm starts by testing the performance of the ship with an angle of attack identical to the first control algorithm. Then, it starts iteratively lowering the angle of attack in steps of 10% of the maximum angle and measures the resulting change in power delivered to the propeller. If the power is reduced by lowering the angle of attack, the search continues, and the effective angle of attack is reduced further. If the power is increased, the search stops and the previous value with the lowest power is used. This algorithm will therefore reduce the angle of attack in cases where the sail-induced resistance is larger than the thrust. The angle of attack is reduced with the same relative amount for all sails for simplicity. This means that the aerodynamic center of effort is mostly kept close to the midship location. The background for this simplification was an analysis of the hydrodynamic models which suggested that the sail-induced resistance is not very sensitive to the exact location of the aerodynamic center of effort. A plot showing this analysis will be given in Section 7.1.1. However, improvements could potentially be achieved by introducing individual reduction factors for each sail. This is a potential topic for future work.

For both control algorithms, the sails are retracted in some weather condition. However, the exact criteria for retracting the sails differ between the algorithms. For the first algorithm, the sails are only retracted if they produce negative thrust. For a control algorithm that does not include hydrodynamic effects, this is the only way to detect when the sails are not useful. For the second algorithm, the sails are retracted whenever they do not decrease the fuel consumption for any of the tested angles. This is measured by comparing the power delivered to the propeller with the sails up against the power with the sails retracted. In cases where the sails are retracted, the effective sail area in the model is reduced to a quarter of the size, and the angle of attack is set to zero. The forces on the sails in these conditions is therefore only the drag estimated from the model at zero angle of attack, which act parallel to the apparent wind.

#### 6.1.3. Dynamic keel control algorithm

The dynamic keel is adjusted based on two rules. The first rule determined when the keel should be deployed. This only happens when the side force from the sails exceeds a minimum value to avoid unnecessary drag. The second rule determines the angle of attack for the keel when it is deployed. This is based on a simple open loop controller that adjusts the angle proportional to the side force from the sails. However, the maximum angle of the keel relative to the ship is also limited to 14°, which corresponds to a lift-coefficient of approximately 1.0 in cases with no drift.

The numerical values of the settings in the control policies are adjusted based on the hydrodynamic model of the hull, rudder, and keel. The proportionality controller was adjusted based on an optimization process where the resistance from the hydrodynamic model was minimized, under the influence of an applied side force. We tested different values for the applied side force that corresponded to 0.5, 1.0, and 2.0 times the straight-ahead resistance of the ship. The values are around the typical values from the sails on the case study route, as will be shown in Section 7.2. We also varied the velocity between 8 and 16 knots. The results from the optimization showed that the sail-induced resistance was lowest when the keel balanced between 50%–51% of the applied side force for the tested conditions. In other words, the optimal relative side force from the keel was not very sensitive to ship speed or the value of the applied side force. The final value in the route simulations was rounded off to 50% for all ship speeds. We also manually verified that balancing 50% of the applied side force was more efficient than a 100%. The former resulted in 25–40% lower sail-induced resistance than the latter, depending on the tested conditions.

The limit for when to deploy the keel was set to the minimum value where there is a positive effect on the total ship resistance. This was found to correspond roughly to 16.7% of the max side force limit for the sails, which was explained in Section 6.1.2. Plots showing the effect on the forces using this control algorithm, as well as the keel angles as a function of the applied side force, are presented in Section 7.1.

### 6.2. Route and weather data

Weather data for the year 2020 was downloaded from the ERA-5 hindcast model from the European Center of Medium range Weather Forecast (ECMWF) (Hersbach et al., 2020). The data consist of wind velocity components 10 m above the sea surface as well as wave data for both wind- and swell-driven waves. The global data is presented on a

Gaussian grid. The data for the route is found by first discretizing the path into equally spaced line segments and then using nearest neighbor interpolation on the global grid for each discrete control point. Fig. 19 shows a map of the route where global grid points are shown together with the discrete grid points making up the route. We downloaded data for the hours 0, 6, 12, and 18 for each day during the year. Since the ship is traveling both to and from Trondheim, each scalar variable – wave height, wave period, directional width, and wind velocity – is added twice to the complete dataset, while directional variables – wind and wave direction – are computed individually for both directions. This resulted in approximately 79 thousand individual weather conditions.

Two operations are used to reduce the complete dataset. First, the worst weather conditions are filtered out as they could represent cases where it is unlikely that a small cargo ship would operate. The exact limit for such cases is somewhat ambiguous. As an estimate, the model for the added resistance in waves is used to calculate when the ship speed is reduced to such a degree that steerability may become an issue. The ship was required to reach at least 7 knots speed with the smallest engine size and without sails in all weather conditions used in the route simulation. This requirement removed around 8% of the worst conditions from the raw data. Second, we randomly picked 10 000 data points from the filtered data to reduce the execution time for each route simulation. The resulting weather statistic are shown Fig. 20 and Fig. 21. The wind data is shown for various ship velocities to illustrate the effect of forward speed on the variables.

## 7. Results

The results are presented in two main subsections. We start with an initial analysis of the hydrodynamic models generated for the various design configurations in Section 7.1. The results quantify how the resistance of the ship depends on the amount of side force from the sails that must be balanced, and whether the added resistance is mainly caused by forces acting on the hull, the rudder, or the keel. The results from the route simulations are then presented in Section 7.2. These results show how much the estimated fuel savings are reduced due to the sail-induced resistance and how large the sail-induced resistance is relative to the other resistance components in the analysis. We also present statistical values for the sail forces and the resulting ship state. Finally, the effect of varying the control strategy is quantified in Section 7.2.4.

### 7.1. Hydrodynamic models

#### 7.1.1. Externally applied side force

The hydrodynamic models of the different design variants are tuned based on a static drift test and static rudder tests with varying propeller loading, as shown in Section 4.1. However, a wind-powered ship needs to balance both the side force and the yaw moment from the sails and will therefore always travel with combination of drift and rudder angles during steady state operation. To give an initial overview of the sail-induced resistance, we have calculated how the ship will respond to an externally applied side force at a ship speed of 12 knots, using the hydrodynamic models. Two different tests are performed. The first test varies the magnitude of the externally applied side force but keep the center of effort fixed at the midship location. This is roughly the location of the aerodynamic center of effort for the forces from the sails with the sail location and control algorithm used in this case study. The second test use a fixed side force equal to two times the straight-ahead resistance of the bare hull and vary the center of effort. The results from both tests are shown in Fig. 22. The y-axis in the figure is the resistance of the ship divided by the calm water straight-ahead resistance of the bare hull as a reference value. The plot to the left show how the resistance varies with the magnitude of the applied side force while the plot to the right show how the resistance is dependent on the center of effort of the applied side force. The lines are only plotted up to the point where the rudder model experiences a lift-coefficient equal to the limit in the sail-control algorithm, presented in Section 6.1.2. The actual operational limit during a route simulation also depends on the propeller thrust, but the results in Fig. 22 give an indication of the maximum side force that is possible to be balanced by the ship when the sails are the main source of thrust.

The results show that the sail-induced resistance can reach values as high as 46% of the straight-ahead resistance for the bare hull before the rudder limit is exceeded. The max side force ratio is estimated to roughly 2.9. Adding the bilge keels or the static high aspect-ratio keel is shown to both increase the max side force and reduce the sail-induced resistance. At a side force ratio of 2.9, the sail-induced resistance is reduced to approximately 37% and 34% of the straight-ahead resistance for the bilge keels and the high aspect-ratio static keel respectively. This constitutes a reduction in the sail-induced resistance of 20% and 26% relative to the sail-induced resistance of the bare hull at the same side force ratio. The fact that the low aspect-ratio bilge keels are roughly as efficient as the high aspect-ratio static keel is interesting. More on that later. Both keel types also increase the straight-ahead resistance with roughly 2.5% due to the increased wetted surface. The dynamic keel has

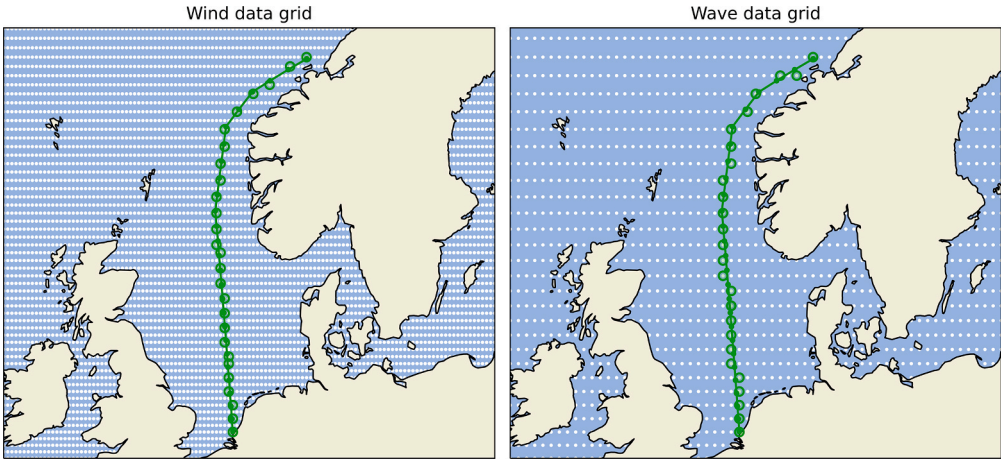


**Fig. 19.** Map of the route on top of the global grid. Each grid point on the global grid is shown as white dots. The green line and smaller dots represent the discretized route. The larger green circles show the nearest neighbors to the route points on the grid. (For interpretation of the references to colour in this figure legend, the reader is referred to the Web version of this article.)

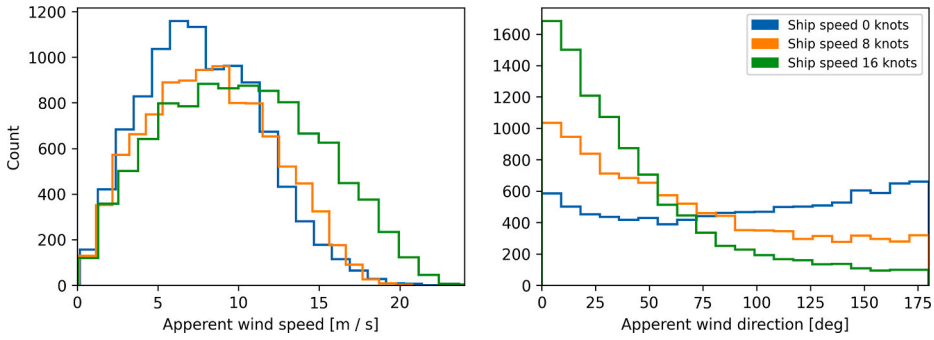


**Fig. 20.** Apparent wind statistics as a function of ship speed.

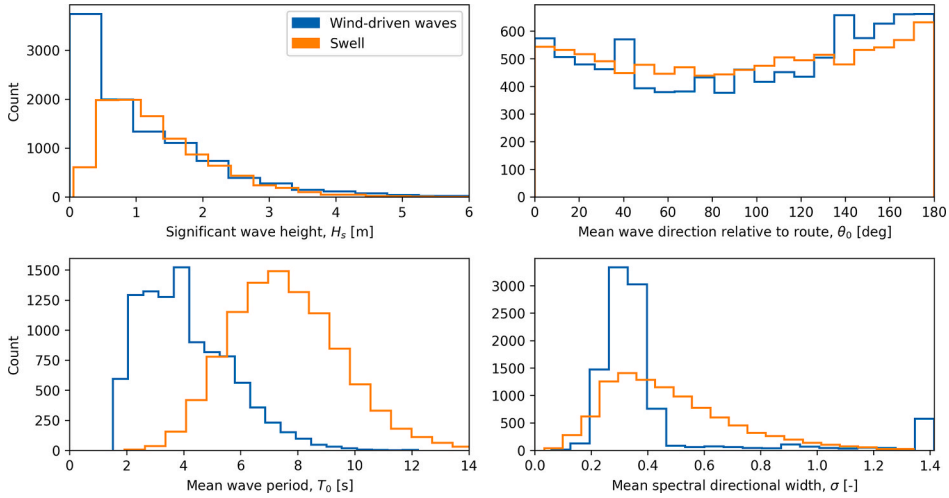


**Fig. 21.** Wave statistics from the dataset used in the route simulations.

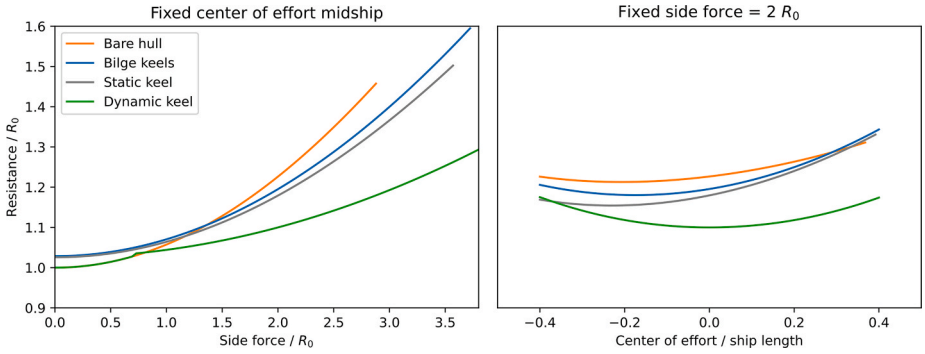


**Fig. 22.** Sail-induced resistance as a function of an externally applied side force. Assumed operational speed is 12 knots and there is no propeller thrust. $R_0$ refers to the straight-ahead resistance of the bare hull, which corresponds to approximately 130 kN.

a much larger impact on the sail-induced resistance. At a side force ratio of 2.9, the sail-induced resistance is reduced to roughly 18% of the straight-ahead resistance, which constitutes an improvement of 61% relative to the bare hull. As the dynamic keel is retractable, the resistance in straight ahead conditions is identical to the bare hull. Although the center of effort of the applied side force does influence the sail-induced resistance, the variation is relatively small. The optimal location is ahead of the midship location for all design variants except the one with the dynamic keel. However, the difference in the resistance between a center of effort midship and the optimal center of effort is only around 1–2%. As mentioned in Section 6.1.2, the sails are not optimized to vary the center of effort during the route simulations, and the aerodynamic center of effort is generally midship for all weather conditions. This simplification was motivated by the results presented in Fig. 22.

The computed values for the drift, rudder, and keel angle as a function of the applied side force with a center of effort midship are shown in Fig. 23. The values are shown both relative to the flow and relative to the ship's center line. In the case of the rudder, the flow angle is estimated from the rudder velocity expressions in the MMG model. For the keel, the angle relative to the flow is the dynamic keel angle plus the drift angle. The plot shows that the drift angle is small relative to the rudder and keel angle, even for large side force ratios. As expected, the keels – static or dynamic – reduce both the drift and rudder angle.

To investigate the source of the resistance, we have divided the hydrodynamic side force and the sail-induced resistance into separate

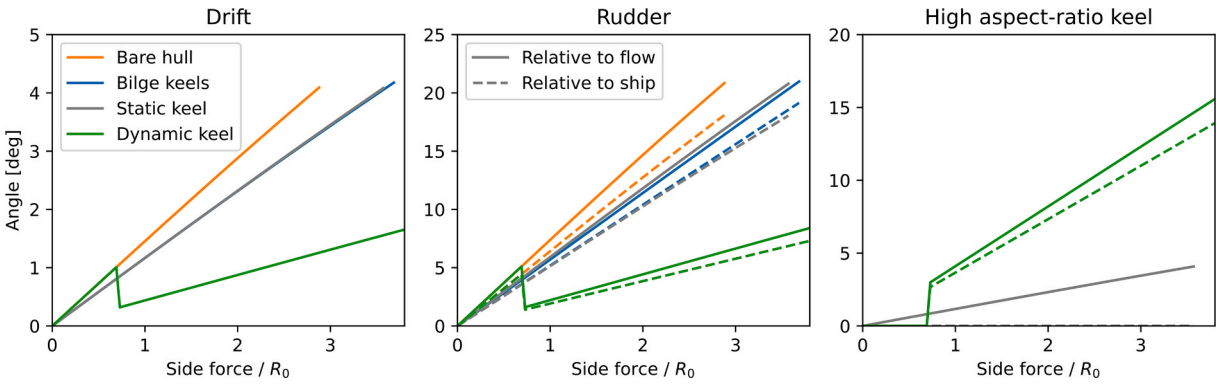


**Fig. 23.** Drift, rudder, and keel angles as a function of an externally applied side force acting midship. Assumed operational speed is 12 knots and there is no propeller thrust. $R_0$ refers to the straight-ahead resistance of the bare hull, which corresponds to approximately 130 kN.

components for the hull, rudder, and keel. The result of this analysis is shown in Fig. 24. The figure shows the magnitude of the forces at a ship speed of 12 knots and a side force ratio of 2.0. This is a case representing a relatively large side force from the sails – as will be shown later Section 7.2.3 and 7.2.4. For both the bare hull and the hull with static keels – low or high aspect-ratio – the rudder is the main source of the added resistance. Despite this, the hull is balancing as much of the hydrodynamic side force as the rudder or more. When the dynamic keel is added, it becomes the main source of both the side force and the sail-induced resistance. The lift-induced drag on the dynamic keel is significantly lower than for the rudder. This is explained by a higher geometrical aspect-ratio than the rudder, but also by the placement of the keel. The rudder is placed in the wake of the hull and close to the skeg which cause significant interaction effects, while the keel is placed at the flat midship section. Consequently, the effective aspect-ratio for the keel model is higher and there is no wake that reduces the lift force. The value of the estimated effective aspect-ratio for the rudder is roughly 1.57, while the same value for the keel is 5.4.

Initially it may seem strange that the hull, which is a lifting surface with a small aspect-ratio, can produce a side force more efficiently than the rudder. However, this is not so strange if the lift coefficients of the two different surfaces are compared. This is done in Fig. 25. For each lifting surface, the lift coefficient is calculated based on the individual representative area and the local velocity, including the wake. As shown in the expressions in Section 4.1.3, lifting line theory predicts that the lift-induced drag is roughly proportional to the lift coefficient squared and the representative area while inversely proportional to the aspect-ratio. The rudder has a geometrical aspect-ratio that is more than 30 times higher than the hull and a planform area that is only 2% of the representative area of the hull. However, at a side force ratio of 2.9, the lift coefficient on the bare hull is only 0.013, while the lift-coefficient on the rudder is close to 1.0. Based on the simplified theory, the lift-induced drag on the rudder should be roughly 3.7 times as high as the lift-induced drag on the hull. For comparison, the hydrodynamic models tuned based on CFD data suggest that the hull is around 3 times as efficient as the rudder. This also explains the effect of the bilge keels and the limited effect of the static high aspect-ratio keel. When the bilge keels are added, more of the side force is shifted from the rudder to the hull. As the hull is a more efficient surface, the total drag is reduced. The static high aspect-ratio keel is shown to have a relatively low lift-coefficient for all side force ratios. This is because the angle of attack of the static keel is dependent on the drift angle of the hull. As a result, to achieve large lift coefficients on a static keel, there must also be large lift on the hull. This problem is solved by the dynamic keel, where the lift on the hull and the keel is separated. The lift coefficient for the dynamic keel is therefore roughly 4 times as high as for the static keel.

### 7.1.2. *Center of lateral resistance*

The reason the static keels can reduce the lift from the rudder is explained by a shift in the center of lateral resistance as a function of drift angle. The variable determines how much the rudder must be actively used to balance the hydrodynamic yaw moment on the ship for a given side force. Theoretically, it is possible to place the sails such that they apply a side force at the location of the center of lateral resistance. In that case, the aerodynamic side force can be balanced by drift-induced forces alone. However, this is often impractical, especially when using several sails. The center of lateral resistance is usually far ahead of the midship location. As an example, the tanker KVLCC2 has a center of lateral resistance that varies between 0.44 and 0.54 ship lengths ahead of the midship location, for drift angle between 3 and 6° (Kume et al., 2006). The work presented in (van der Kolk et al., 2021) shows experimental values for a ship with varying configurations of bilge keels. The

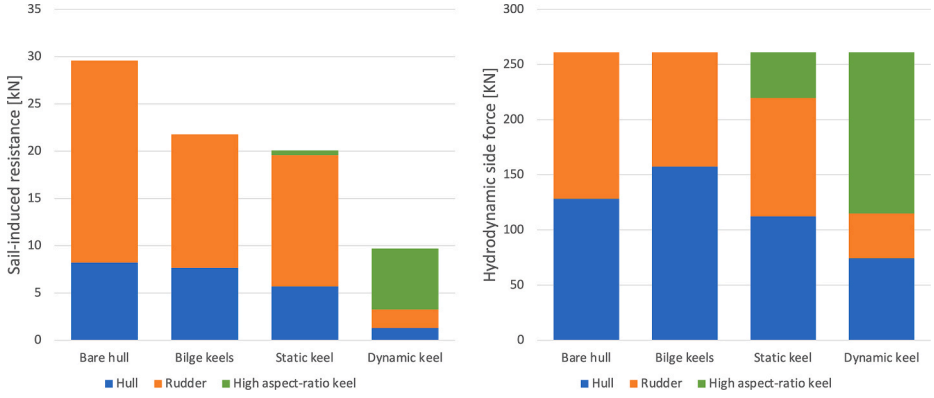


**Fig. 24.** Division of the sail-induced resistance and the hydrodynamic side force into different components for the hull, rudder, and keel. The values in the figure are for a ship speed of 12 knots and a side force ratio of 2.

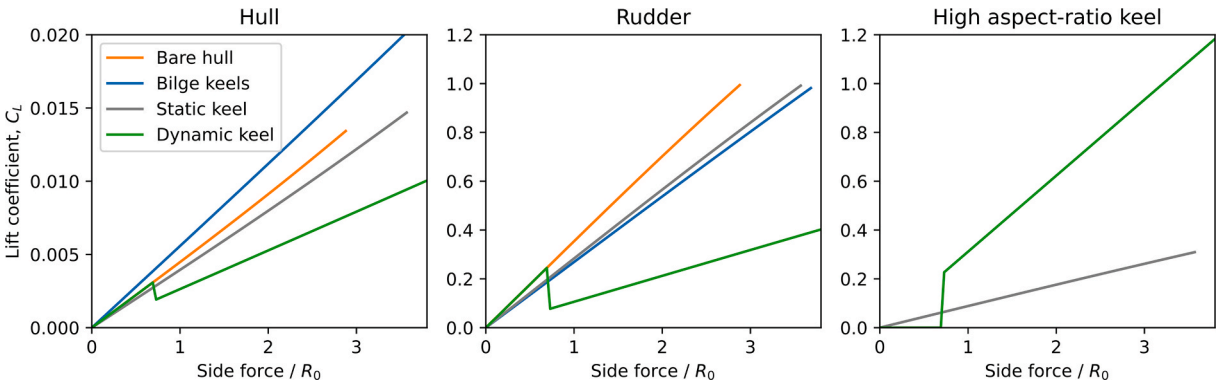


**Fig. 25.** Lift coefficient of the different lifting surfaces making up the ship.

main dimensions and shape of the ship are similar to the one in this study. The exact value for the center of lateral resistance varies as a function of the bilge keel configuration but is mostly seen to be ahead of the bow. For the most extreme cases it is seen to be an entire ship length ahead of the midship location. Adding the bilge keels generally moved the center of lateral resistance close to, but not always behind, the bow. The center of lateral resistance for the ship in this study is plotted in Fig. 26 for the static design variants. The location is calculated by dividing the hydrodynamic yaw moment acting on the hull and the rudder by the sway force. The location is then made non-dimensional by the ship length. The bare hull in this case study is seen to have a center of lateral resistance ahead of the bow. Both the bilge keels and the high aspect-ratio keel is seen to shift the center of lateral resistance backwards with similar magnitude. However, the location is relatively close to the bow for all versions.

### 7.2. Route simulations

Three different route simulations are used for each combination of design configuration, number of sails, and velocity. First, the ship is tested without sails to generate reference data on the resistance and propulsion power. The route simulation is necessary in this case to quantify the effect of the added resistance in waves. The ship is then tested with a modified sail model where the side force and yaw moment are neglected which also removes the sail-induced resistance. The sails are still affected by the side force limit, but not the limits on the rudder and heel angle. The propeller efficiency is calculated as a function of the required thrust. This gives a theoretical maximum value for the fuel savings if the side force could be balanced without any added resistance. Finally, the ship is tested with all hydrodynamic effects included. The thrust, side force, yaw moment, and heel moment from the sails are balanced by opposing hydrodynamic forces and moments on the hull.

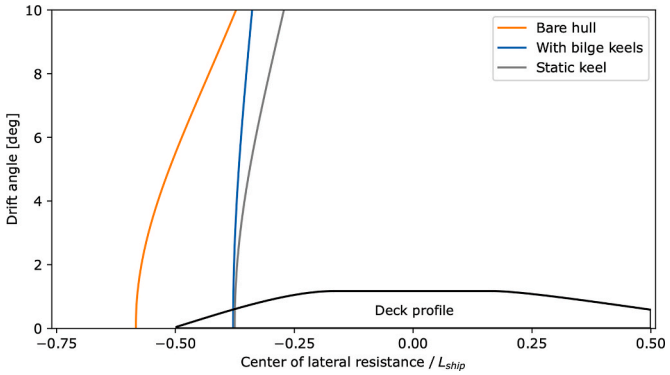


**Fig. 26.** Center of lateral resistance for the hydrodynamic side force as a function of drift angle.

The sail control algorithm is affected by the response of the ship. We present the results from these route simulations in the following sections. The first sections show results with the max thrust control algorithm as outlined in Section 6.2.1. We then show the consequence of including hydrodynamic effects in the algorithm and altering the side force limit in Section 7.2.4. The presentation of design configurations is limited to the bare hull, the hull with bilge keels, and the dynamic keel. This is because the results for the high aspect-ratio static keel are almost identical to the results for bilge keels.

#### 7.2.1. Fuel savings

The fuel saving on the route for a given test condition is defined as the reduction in the average propeller power when sails are used, relative to a simulation with the bare hull, but without sails. Fig. 27 shows the values both with all hydrodynamic effects included in the simulation and with the side force and yaw moment neglected. The fuel savings due to sails are estimated to be between 21 and 71% without hydrodynamic effects, depending on the number of sails, ship speed and design configuration. With hydrodynamic effects included, the numbers are reduced to 17–65%. The reduction in the fuel savings due to hydrodynamic effects are seen to be between 4.1 and 10.8 percentage points. The reduction is largest for the bare hull, at either low ship speed or many sails, but is also clearly visible for the other configurations. Adding the bilge keels is not seen to improve the fuel savings relative to the bare hull configuration. The sail-induced resistance is reduced – as shown in Section 7.1 and 7.2.3 – but the added frictional resistance in straight ahead conditions is just large enough to cancel out the positive effect. The dynamic keel is seen to increase the fuel savings with 4.5 percentage points for the lowest speed. The reduction in fuel savings due to hydrodynamic effects is thereby only 6.3 percentage points.

When the number of sails is fixed to three, the fuel savings are reduced with increasing ship speed due to the increase in hydrodynamic resistance. When the velocity is fixed, the fuel savings increase with the number of sails. However, there is a clear effect of diminishing returns when adding more sails. This happens both with and without sail-induced resistance included in the model. The explanation is that some wind directions offer significantly more thrust than others, as shown in Fig. 17. When the total sail area is small, the energy extracted from all wind directions can be increased by increasing the number of sails. At some point, the most favorable wind directions are completely utilized, and adding more sail area only increases the fuel savings during the less favorable wind conditions. These wind conditions offer less fuel savings per sail area, and the effect of increasing the number of sails is therefore smaller.

#### 7.2.2. Resistance components

The average values for all resistance components in the route simulation are shown in Fig. 28. The sail-induced resistance is seen to be between 4.6% and 14.2% of the total resistance depending on the ship

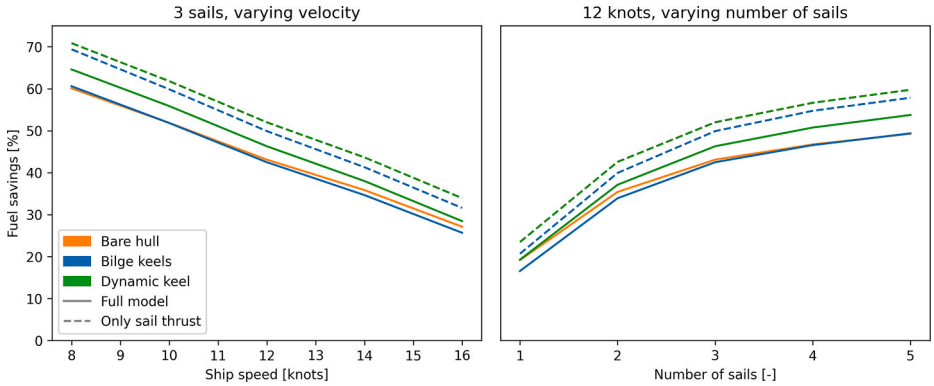


**Fig. 27.** Fuel savings on the ship as a function of velocity and number of sails.

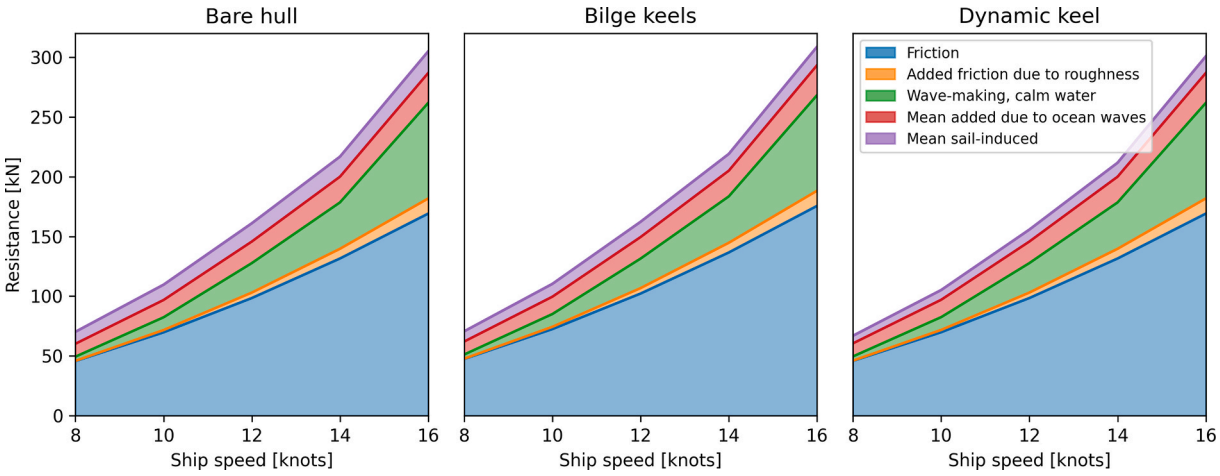


**Fig. 28.** Resistance components for the ship with three sails.

speed. As a comparison, the magnitude is around the same value as the estimated added resistance due to waves for the bare hull. Although the calm water resistance is still the largest source of resistance for all the tested speeds, the lowest speeds are particularly affected by weather induced resistance components. The added resistance in waves and the sail-induced resistance accounts for 29.6% of the total resistance at 8

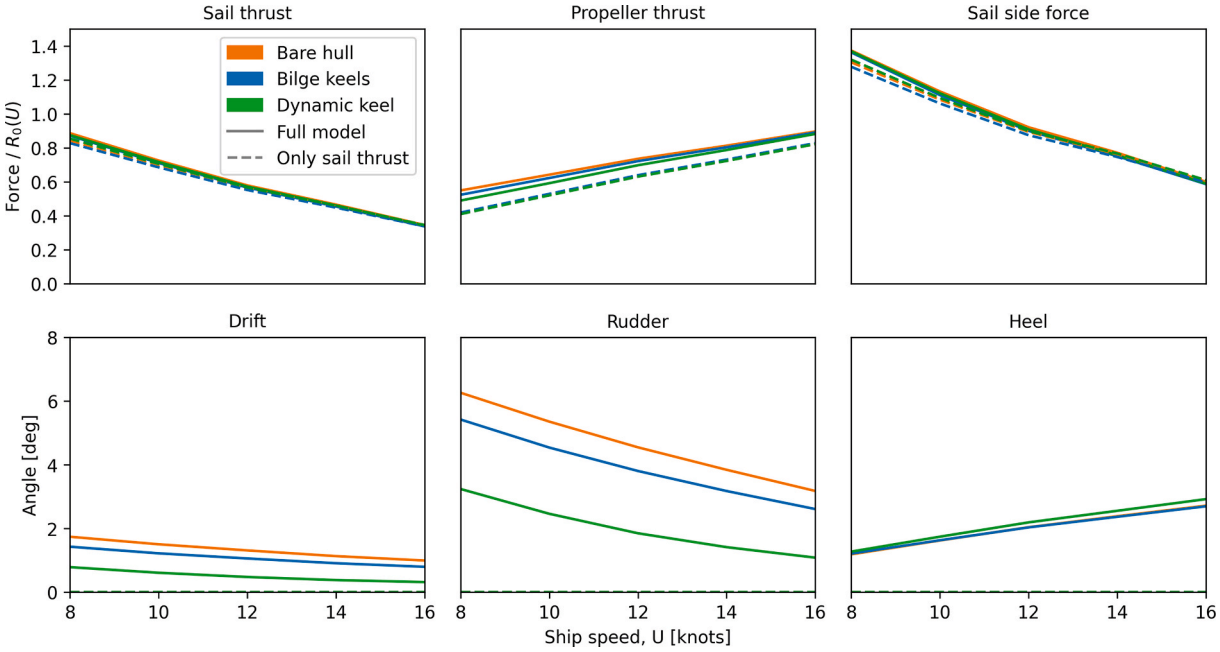


**Fig. 29.** Average ship state with three sails and variable ship speed.

knots while only 14.1% at 16 knots. This is partly because the case with lowest speed experiences the largest sail forces relative to the ship resistance, but also because the added resistance due to waves does not change much with ship speed. Similar conclusions regarding the added resistance in waves are made in (Taskar and Andersen, 2020). The relative reduction in fuel savings and the relative importance of the sail-induced resistance is similar in magnitude. This suggests that the increase in resistance is the main reason for the reduction in fuel savings, and not changes in the operational angle of attack on the sails – for instance due to the rudder limit. For the lowest speed, the sail induced resistance for the bare hull, the hull with bilge keels and the dynamic keel is 14.2%, 12.1% and 9.5% respectively. This shows that the bilge keels and the dynamic keel reduce the average sail-induced resistance with almost 15% and 33%.

#### 7.2.3. Model state overview

Average statistical values for sail forces, propeller thrust, drift, rudder and heel angle are plotted in Fig. 29. The force values are shown relative to the straight-ahead resistance of the ship as a function of velocity – which is equal to the sum of the frictional resistance, the added friction due to roughness and wave-making resistance in Fig. 28. The results show that both the thrust and the side force from the sails are slightly increased when sail-induced effects are included in the route simulation. This is because the resistance of the ship increases, which makes the sails operate with larger angles of attack in cases where the max angle is not already reached. The average values of the side force vary between 0.6 and 1.4 times the straight-ahead resistance. This is in many ways a relatively moderate value if we compare this value to the results in Fig. 22. The lift-coefficient on both the rudder and the hull is low and the ship is operating far from the limits in the control algorithm for the sails. However, these are only average values, and there are several situations where the limits come into play. This will be further explored later. The drift and rudder angles are decreasing with increasing ship speed. This is because the hydrodynamic forces are proportional to the ship velocity squared, and the ship is therefore capable of balancing larger aerodynamic side forces at higher velocity. Both the drift and the rudder angle are reduced when the keels are added. The hydrostatic moment on the hull is not affected by hydrodynamic effects and the heel angle is therefore increasing with the velocity. As mentioned in Section 2.1.3, the rudder and the keel generate a hydrodynamic heel moment that is proportional to the side force they produce and a fixed vertical center of effort. However, the added heel angle due to the appendices is small for this case study as the hydrostatic moment on the hull is dominating the restoring moment. As an example, the average increase in heel angle due to the dynamic keel was less than 0.3° at 16 knots. With increasing speed, the sail forces are reduced relative to the ship resistance, but they are increased in absolute value. As an example, the average side force from the sails at 16 knots is around 3.9 times larger than the value at 8 knots. The reason is that the increase in ship velocity also increases the apparent wind velocity and decreases the apparent wind angle, as shown in Fig. 20.

An overview of the heel angle and the propeller operating conditions for the bare hull configuration is presented in Fig. 30 and Fig. 31. The results are very similar for all configurations since both the hydrostatic hull model and the propeller model are identical between the design configurations. The only ship speed where the heel angle is affecting the sail control algorithm is 16 knots. For 8 knots, the maximum heel angle is only 4°. Although this is data for a ship with a relatively high stability, it shows that large fuel savings can be possible for merchant ships without significant heel angles. The propeller is seen to mostly operate around the design point, although there are a few cases where the efficiency is reduced considerably due to a high advance ratio. However, this only happens for cases with very small amount of thrust from the propeller and the effect of this is therefore small. As a sidenote, such high advance ratios might lead to risk of damaging pressure-side cavitation on the propeller and might be a reason to use a variable pitch propeller.

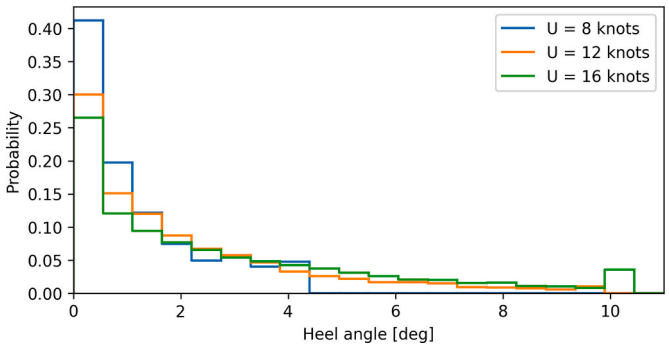


**Fig. 30.** Statistics for the heel angle during the route simulation. The results are shown for the bare hull.

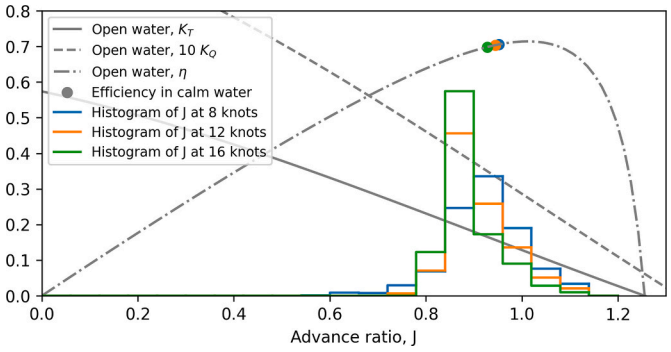


**Fig. 31.** Statistics for the propeller advance ratio plotted on top of the open water characteristics for the propeller.

However, this is outside the scope of the present study.

#### 7.2.4. Adjustments to the control algorithm

The route simulation results presented in the previous sections were computed with the control strategy that maximized the thrust from the sails, and with the largest side force limit, as explained in Section 6.1.2. In this section, we also include the control algorithm that iteratively optimize the angle of attack by evaluating the hydrodynamic performance of the ship. Both control strategies are tested with varying values for the side force limit. The variation in the side force limit serves two purposes. First, it is a simple way to modify the max thrust control algorithm to avoid situations with large sail-induced resistance. We wanted to test if a reduction in the side force limit could lead to better fuel savings without any other changes to the control algorithm. Second, even if the fuel savings are not improved by reducing the side force limit, it could still be beneficial to ensure low side forces from the sails. This could for instance be a way to achieve better steerability of the ship or to avoid large heel angles. In this case, it is useful to quantify any loss in the fuel savings due to more strict limits on the sail forces.

Fig. 32 shows the averaged statistical values for the fuel savings, the thrust from the sails, and the sail-induced resistance as a function of different values for the side force limit in the control algorithm. For the control strategy study, we limit the presentation to the case with 8 knots ship speed and three sails. This was the case with both the largest fuel savings and the largest reduction due to hydrodynamic effects. It is a case where the rudder is operating with angles close to the rudder limit relatively often – as will be shown later - while the max heel limit is never reached. The max thrust control algorithm with an optimal side force limit results in an estimated fuel saving that is only 1% less than the hydro optimized control algorithm for the bare hull. This result is slightly different than our previous study found in (Kramer and Steen, 2016). In the previous paper, a control algorithm optimized with hydrodynamic effects included in the objective function showed

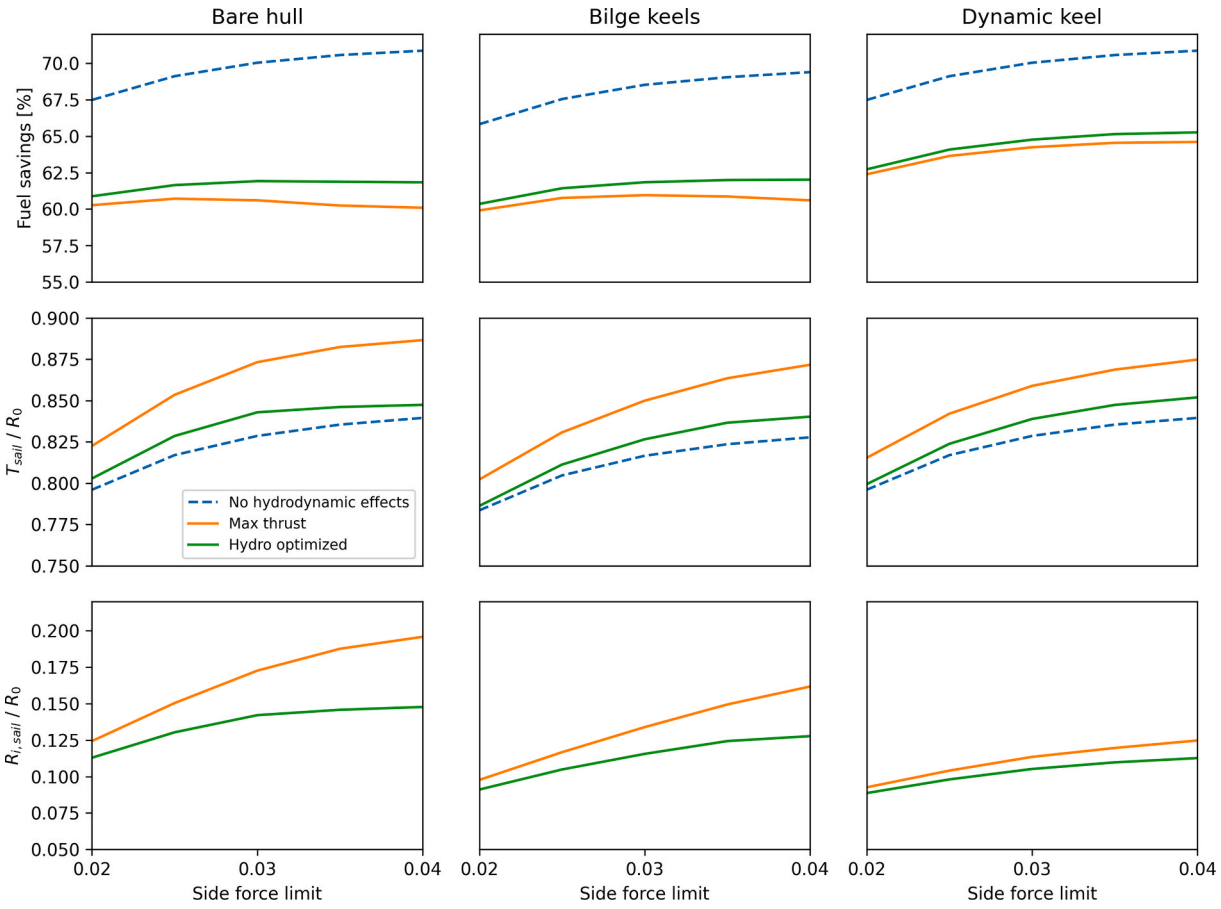


**Fig. 32.** Fuel savings, sail thrust, labeled $T_{sail}$, and sail-induced resistance, labeled $R_{i,sail}$, as a function of the side force limit in the control algorithm. The data is from cases with 8 knots ship speed and 3 sails.

improvements to the fuel savings that approached 5%, for a case with close to 50% fuel savings. However, an important difference between the previous study and this one is the limits on the rudder lift coefficient and the side force. The previous study simulated a ship that in some situations operated with a much larger side force than the current case, and the benefit of including hydrodynamic effects in the control algorithm was therefore larger. As seen in this study, the difference between the two control algorithms increases with increasing side force limit. This indicate that a simple max thrust control algorithm combined with a correct side force limit can be almost as good as a hydrodynamically optimized control algorithm. Another interesting observation is that the fuel savings are not very sensitive to the side force limit within the tested range. Even though the thrust from the sails is reduced with roughly 6.4% with the changing side force limit, the fuel savings are changed with less than 1% for the bare hull. The explanation is found in the change in the sail-induced resistance; it is shown to be reduced almost as much as the sail thrust. The drawback with strict limits on the side force is therefore seen to be small for this case. The effect is different for the configuration with the dynamic keel, which shows larger reduction in the estimated fuel savings along with the side force limit. This is because the keel is capable of balancing larger side forces without too much sail-induced resistance.

Fig. 33 shows a scatter plot of both the rudder angle and sail thrust as a function of the side force from the sails. This figure shows the spread in the variables during the route simulations and illustrate the consequence of the different control algorithms. For both algorithms, the figure shows how the variables are affected by the side force limit. For the largest side force limit the operation is also affected by the limit on the rudder lift coefficient which are visible by the maximum angle for the rudder. The spread in the rudder angle for a given side force is mainly due to the variability in the propeller thrust which again are dependent on the variability in the sail thrust. For a given side force ratio, there are situations with both large and small amounts of thrust and therefore both small and large thrust loading coefficients. When the max thrust control algorithm is used, there are several occasions where the thrust from the sails is smaller than the sail-induced resistance. With the hydro optimized control algorithm, the angle of attack on the sails is reduced in these situations, so that the thrust is always larger than the sail-induced resistance.

Fig. 34 shows scatter plots for the geometric angle of attack averaged over all three sails as a function of the apparent wind angles in the route simulation. Each plot is limited to apparent wind angles between 0 and 30° as the difference between the control algorithms is mostly seen in this range. This is also the range where the sails produce the largest side forces relative to the thrust. The max thrust control algorithm with the largest side force limit is seen in the plot to the left. When lowering the side force limit in the middle plot, the angles of attack are shifted fairly evenly downward. The change is different when the angles of attack are optimized with hydrodynamics in the objective function, as shown to the right. At apparent wind angles less than 10°, the angles of attack of the sails are reduced more with the hydro optimized control algorithm than when reducing the side force limit. For the other apparent wind angles, they are reduced less. There are also clear patterns in the hydro optimized data. This is a result of the discrete jumps of the angles that are tested in the hydro optimized control algorithm, as outlined in Section 6.1.2.

## 8. Conclusions

We performed a case study of a wind-powered cargo ship operating

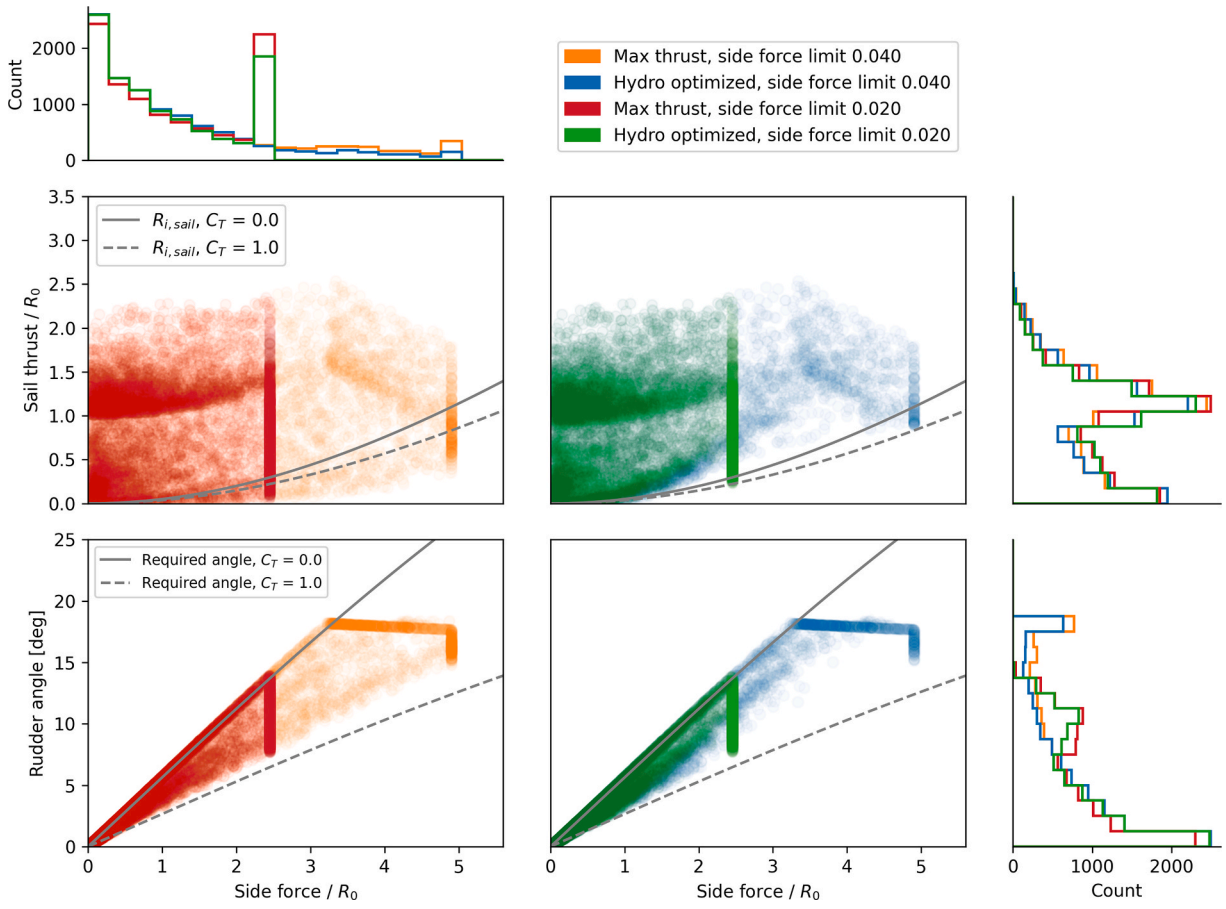


**Fig. 33.** Overview of sail thrust and rudder angle for a selection of different route simulations with 8 knots ship speed and 3 sails.

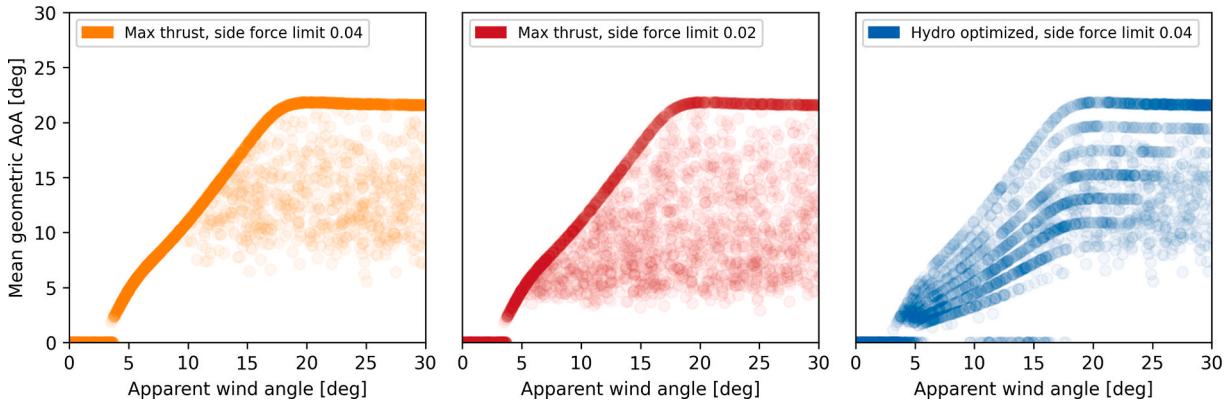


**Fig. 34.** Average geometric angle of attack for the sails as a function of apparent wind angles in the route simulation.

on a route in the north Atlantic by combining hydrodynamic CFD simulations, route simulation models based on maneuvering theory, and a discrete lifting line model for the wingsails. The goal was to investigate the magnitude and the source of the sail-induced resistance. We tested four different design configurations and varied both the operational speed, number of sails, and the control algorithm for the sails. The cases tested gave an estimated fuel savings between 17 and 65%.

The sail-induced resistance for the bare hull was found to be between 4.6 and 14.2% of the total resistance in the route simulations, depending on the ship speed, hydrodynamic design, and number of sails installed. This led to a reduction in the fuel savings that roughly corresponded to the relative increase in resistance. As a comparison, the sail-induced resistance was comparable to the estimated added resistance in waves for the bare hull. At 8 knots – the lowest ship speed tested – the sum of the sail-induced resistance and added resistance in waves accounted for roughly a third of the total resistance on average. This showed that the error in the estimated fuel consumption of a wind-powered cargo ship can be large if only the calm water resistance is used to quantify the energy requirements.

Although both the hull and the rudder contributed significantly to the side force, the rudder was found to be the main source of sail-induced resistance for three of the four design configurations tested. The reason was that the rudder was operating with very large lift-coefficients, which resulted in large lift-induced drag forces. The exception was the design configuration with the dynamic keel. In that case, the keel took over as the main source of both resistance and side

force.

The design configurations where first analyzed independently of the sail model and weather data. As a simplified analysis of the sail-induced resistance, they were subjected to a side force with varying magnitude applied at the midship location. This analysis showed that the bilge keels and the static keel would give similar reductions in the sail-induced resistance relative to the bare hull. As an example, the relative reduction was 20% and 26% for the bilge keels and the static keel when the ship was balancing a side force that was 2.9 times the straight-ahead resistance. This was mainly achieved by shifting some of the hydrodynamic side force from the rudder to the hull and keel, and thereby reducing the lift-coefficient on the rudder. The dynamic keel was able to reduce the sail-induced resistance with 61% relative to the bare hull when the same side force was applied. This was achieved by offloading both the rudder and the hull at the same time. The control algorithm for the dynamic keel was optimized to minimize the sail-induced resistance. The optimization result indicated that the keel should balance roughly 50% of the total side force. Although the dynamic keel represents a much more complex solution than the static keels, it could be worth considering for cases where a very large amount of power is to be extracted from the wind.

The amount of side force from the sails in the route simulations was naturally varying depending on the weather, but the average value was close to 0.6–1.4 times the straight-ahead resistance, depending on ship speed and number of sails. The bilge keels did not improve the fuel savings from the sails, as the average reduction in sail-induced resistance was about the same as the increase in the frictional resistance. The dynamic keel, on the other hand, was able to improve the fuel savings with 4.5 percentage points for the case with the largest fuel savings. This was achieved by reducing the average sail-induced resistance with 33%. Since the keel was retractable, it did not increase the straight-ahead resistance for cases with low side forces from the sails.

The tests were done with control algorithms that were designed to include various limits on the angle of attack of the sails to avoid dangerous situations for the ship. This meant that the forces from the sails were reduced in the most extreme weather situations in all tested conditions. The estimated fuel savings were therefore not very dependent on the variations in the different control algorithms tested. However, the sail-induced resistance and the thrust from the sails showed much larger variations. Limiting the side force from the sails through the control algorithm was found to reduce the sail-induced resistance roughly as much as the reduction in the wind generated thrust, depending on the hydrodynamic ship design. The conclusion is therefore that the case study ship in this paper can be operated with strict limits on the side force while still maintain large fuel savings. This means that both the heel and the rudder angle can be kept at low values, without decreasing the performance from the sails. The best control algorithm was the one that optimized the ship with the negative hydrodynamic effects included in the objective function. However, the simpler control algorithm, that primarily maximized the thrust, were found to be almost as good as the hydrodynamically optimized control strategy.

## CRediT authorship contribution statement

**Jarle Vinje Kramer:** Conceptualization, Methodology, Software, Writing. **Sverre Steen:** Conceptualization.

## Declaration of competing interest

The authors declare that they have no known competing financial interests or personal relationships that could have appeared to influence the work reported in this paper.

## Acknowledgments

This work was carried out at SFI Smart Maritime (WP2) supported by the Research Council of Norway through the Center for Research-based Innovation (SFI)scheme (Grant number 237917).

## References

Amini, H., Sileo, L., Steen, S., 2012. Numerical calculations of propeller shaft loads on azimuth propulsors in oblique inflow. J. Mar. Sci. Technol. 17, 403–421.
Anderson, J.D., 1991. *Fundamentals Of Aerodynamics.* s.L. McGraw-Hill.
Aubin, Nicolas, Augier, Benoit, Sacher, Matthieu, Bot, Patrick, Hauville, Frederic, Flay, Richard G.J., 2017. Wind tunnel investigation of dynamic trimming on upwind sail aerodynamics. J. Sail. Technol. 2 (1).
Ayro, 2022. OceanWing information page [Online] Available at: https://ayro.fr/oceanwing/.
Bentin, Marcus, et al Bentin, M., et al., 2016. A new routing optimization tool-influence of wind and waves on fuel consumption of ships with and without wind assisted ship propulsion systems. Transport. Res. Proced. 14, 153–162.
Bertram, V., 2012. Practical Ship Hydrodynamics. Elsevier, Oxford.
Blount, H., Protell, J.M., 2021. CFD Investigation of Wind Powered Ships under Extreme Conditions. Chalmers Univerusty of Technology, Gothenburg, Sweden.
Bøckmann, E., Steen, S., Myrhaug, D., 2014. Performance of a Ship Powered Purely by Renewable Energy. International Conference on Offshore Mechanics and Arctic Engineering, San Fransisco, California, USA.
Bordogna, G., 2020. Aerodynamics of Wind-Assisted Ships. Delft Univeristy of Technology, Delt, Netherlands.
DNV, 2014. *Environmental Conditions And Environmental Loads - Recommended Practice - DNV-RP-C25,* s.L. DNV.
DNV-GL, 2016. *Rules for Classification, Part 3 Hull, Chapter 15 Stability,* s.L. DNV-GL.
Duport, C., et al., 2017. *Local Results Verification Of a 3D Non-linear Lifting Line Method For Fluid-Structure Interactions Simulation On a Towing Kite For Vessels.* Zevenwacht, High-Performance Marine Vehicles.
Eca, L., Hoekstra, M., 2008. The numerical friction line. J. Mar. Sci. Technol. 13, 328–345.
Econowind, 2020. *Key wind-assist propulsion installation starts North Sea oper*ations [Online] Available at: https://www.econowind.nl/index.php/2020/03/02/key-wind-assist-propulsion-installation-starts-north-sea-operations/. (Accessed 16 August 2021).
ESI-Group, 2020. OpenFOAM homepage [Online] Available at: https://www.openfoam.com/. (Accessed 14 October 2020).
Goldstein, S., 1929. On the vortex theory of screw propellers. Proc. R. Soc. Lond. - Ser. A Contain. Pap. a Math. Phys. Character 123 (792), 440–465.
Hersbach, H., et al., 2020. The ERA5 Global Reanalysis. Quarterly Journal of the Royal Meteorological Society.
Hirt, C.W., Nichols, B.D., 1981. Volume of fluid (VOF) method for the dynamics of free boundaries. J. Comput. Phys. 39 (1), 201–225.
Hunsaker, D.F., 2011. *A Numerical Lifting-Line Method Using Horseshoe Vortex Sheets,* s.L. Utah State Univeristy.
International Towing Tank Conference (ITTC), 2017a. 1978 ITTC Performance Prediction Method, s.L. International Towing Tank Conference (ITTC).
International Towing Tank Conference, 2017b. Laboratory Modelling of Multidirectional Irregular Wave Spectra. s.l., s.n.
International Towing Tank Conference, 2017c. Uncertainty Analysis in CFD Verification and Validation, Methodology and Procedures, s.L. International Towing Tank Conference.
Katz, J., Plotkin, A., 2001. *Low-Speed Aerodynamics.* s.L. Cambridge Univeristy Press.
Kramer, J.V., 2021. Hydrodynamic test programe repository [Online] Available at: https://github.com/jarlekramer/Hydrodynamic-test-program-for-wind-power/.
Kramer, J., Steen, S., 2016. *Drift Forces – Wingsails Vs Flettner Rotors.* Cortona, Italy, High-Performance Marine Vehicles.
Kramer, J.V., Steen, S., 2022. Simplified test program for hydrodynamic CFD simulations of wind-powered cargo ships. Ocean Eng. 244.
Kramer, J.V., Godø, J.M.K., Steen, S., 2018. Hydrofoil simulations – non-linear lifting line vs CFD. In: Cortona, Numerical Towing Tank Symposium.
Kume, K.a.H.J.a.T.Y., Fujisawa, J., Fukasawa, R., Hinatsu, M., 2006. Measurements of hydrodynamic forces, surface pressure, and wake for obliquely towed tanker model and uncertainty analysis for CFD validation. J. Mar. Sci. Technol. 11 (2), 65–75.
Lanchester, F.W., 1907. Aerodynamics: Constituting the First Volume of a Complete Work on Aerial Flight. s.l.. Constable.
Larsson, L., Eliasson, R.E., Orych, M., 2000. Principles of Yach Design. s.l., Bloomsbury.
Liu, S., Papanikolao, A., 2020. Regression analysis of experimental data for added resistance in waves of arbitrary heading and development of a semi-empirical formula. Ocean Eng. 206.
Lu, R., Ringsberg, J.W., 2020. Ship energy performance study of three wind- assisted ship propulsion technologies including a parametric study of the Flettner rotor technology. Ships Offshore Struct. 15 (3), 249–258.
Marien, Wallenius, Laval, Alfa, 2021. The wind-power solution demonstrated in a vessel concept [Online] Available at: https://www.theoceanbird.com/the-vessel/. (Accessed 16 August 2021).
Maskew, B., 1987. *VSAERO Theory Document,* s.L. NASA.
Menter, F., Kuntz, M., Langtry, R., 2003. Ten years of industrial experience with the SST turbulence model. In: Turbulence, heat and mass transfer, 4, pp. 625–632, 1.
Michelin, 2021. 2021 Movin'On: Michelin presents two innovations to accelerate the development of sustainable mobility [Online] Available at: https://www.michelin.com/en/press-releases/2021-movinon-michelin-presents-two-innovations-to-accelerate-the-development-of-sustainable-mobility/. (Accessed 30 December 2021).

Minami, Y., Nimura, T., Fujiwara, T., Ueno, M., 2003. Honolulu, Hawaii, USA. In: Investigation into Underwater Fin Arrangement Effect on Steady Sailing Characteristics of a Sail Assisted Ship. The Thirteenth International Offshore and Polar Engineering Conference.
Oosterveld, M.W.C., Oossanen, P.V., 1975. Further computer-analyzed data of the wageningen B-screw series. Int. Shipbuild. Prog. 22 (251).
Ouchi, K., Uzawa, K., Kanai, A., 2011. Hamburg, Germany. In: Huge Hard Wing Sails for the Propulsor of Next Generation Sailing Vessel (The Second International Symposium on Marine Propulsors).
Perić, R., Abdel-Maksoud, M., 2016. Reliable damping of free-surface waves in numerical simulations. Ship Technol. Res. 63 (1), 1–13.
Phillips, W.F., Snyder, D.O., 2000. Modern adaptation of Prandtl's classic lifting-line theory. J. Aircraft 37 (4), 662–670.
Popovac, M., Hanjalic, K., 2007. Compound wall treatment for RANS computation of complex turbulent flows and heat transfer. Flow, Turbul. Combust. 78 (2), 177–202.
Prandtl, L., 1918. *Tragflügeltheorie.* s.L. Königliche Gesellschaft der Wissenschaften zu Göttingen.
Rumsey, C.L., Slotnick, J.P., Sclafani, A.J., 2019. Overview and summary of the third AIAA high lift prediction workshop. J. Aircraft 56 (2).
Sacher, M., Hauville, F., Bot, P., Durand, M., 2015. Sail trimming FSI simulation-comparison of viscous and inviscid flow models to optimise upwind sails trim. In: Auckland, New-Zealand, 5th High Performance Yacht Design Conference.
Schlichting, H., 1979. *Boundary-Layer Theory*. s.L. McGraw-Hill.
Schneekluth, H., Bertram, V., 1998. Ship Design for Efficiency and Economy. Butterworth-Heinemann, Oxford.
Sheldahl, R.E., Klimas, P.C., 1981. Aerodynamic Characteristics of Seven Symmetrical Airfoil Section through 180-Degree Angle of Attack for Use in Aerodynamic Analysis of Vertical Axis Wind Turbines. Sandia National Laboratories, Albuquerque, New Mexico, USA.
Ship Technology, 2021. Norsepower fits first tiltable rotor sails on SC connector [Online] Available at: https://www.ship-technology.com/news/norsepower-rotor-sails-sc-connector/. (Accessed August 2021).
Spalart, P.R., Rumsey, C.L., 2007. Effective inflow conditions for turbulence models in aerodynamic calculations. AIAA J. 45 (10), 2544–2553.
Talluri, L., et al., 2016. Techno economic and environmental assessment of wind assisted marine propulsion systems. Ocean Eng. 121, 301–311.
Talluri, L., Nalianda, D., Giuliani, E., 2018. Techno economic and environmental assessment of Flettner rotors for marine propulsion. Ocean Eng. 154, 1–15.
Taskar, B., Andersen, P., 2020. Benefit of speed reduction for ships in different weather conditions. Transport. Res. Part D 85.
Tillig, F., Ringsberg, J.W., 2020. Design, operation and analysis of wind-assisted cargo ships. Ocean Engineering 211.
Traut, M., et al., 2014. Propulsive power contribution of a kite and a Flettner rotor on selected shipping routes. Appl. Energy 113, 362–372.
van der Kolk, N.J., et al., 2019. Case Study: Wind-Assisted Ship Propulsion Performance Prediction, Routing, and Economic Modelling. International Conference Power & Propulsion Alternatives for Ships, London, UK.
van der Kolk, I., Akkerman, I., Keuning, J., Huijsmans, R., 2020. Part 2: simulation methodology and numerical uncertainty for RANS-CFD for the hydrodynamics of wind-assisted ships operating at leeway angles. Ocean Eng. 201.
van der Kolk, N.J., Akkerman, I., Keuning, J.A., Huijsmans, R.H.M., 2021. Low-aspect ratio appendages for wind-assisted ships. J. Mar. Sci. Technol. 1–18.
Virtanen, P., Al, E., 2020. SciPy 1.0: fundamental algorithms for scientific computing in Python. Nat. Methods 17, 261–272.
Yasukawa, H., Yoshimura, Y., 2015. Introduction of MMG standard method for ship maneuvering predictions. J. Mar. Sci. Technol. 20 (1), 37–52.
Yuankui, L., Yingjun, Z., Feixiang, Z., 2014. Minimal time route for wind-assisted ships. Mar. Technol. Soc. J. 48 (3), 115–124.